A Network of Conserved Interactions Regulates the Allosteric Signal in a Glutamine Amidotransferase†

Rommie E. Amaro,‡,||,# Anurag Sethi,‡,# Rebecca S. Myers,§,⊥ V. Jo Davisson,§ and Zaida A. Luthey-Schulten*,‡

Department of Chemistry, University of Illinois at Urbana-Champaign, Urbana, Illinois 61801, and Department of Medicinal Chemistry & Molecular Pharmacology, Purdue University, West Lafayette, Indiana 47907

Received August 21, 2006; Revised Manuscript Received October 19, 2006

ABSTRACT: We have combined equilibrium and steered molecular dynamics (SMD) simulations with principal component and correlation analyses to probe the mechanism of allosteric regulation in imidazole glycerol phosphate (IGP) synthase. An evolutionary analysis of IGP synthase revealed a conserved network of interactions leading from the effector binding site to the glutaminase active site, forming conserved communication pathways between the remote active sites. SMD simulations of the undocking of the ribonucleotide effector N^1-[(5′-phosphoribulosyl)-formino]-5′-aminoimidazole carboxamide ribonucleotide (PRFAR) resulted in a large scale hinge-opening motion at the interface. Principal component analysis and a correlation analysis of the equilibration protein motion indicate that the dynamics involved in the allosteric transition are mediated by coupled motion between sites that are more than 25 Å apart. Furthermore, conserved residues at the substrate-binding site, within the barrel, and at the interface were found to exhibit highly correlated motion during the allosteric transition. The coupled motion between PRFAR unbinding and the directed opening of the interface is interpreted in combination with kinetic assays for the wild-type and mutant systems to develop a model of allosteric regulation in IGP synthase that is monitored and investigated with atomic resolution.

Unraveling the intricate details of allosteric regulation has been an active and somewhat controversial area of study for over 40 years. Yet, despite numerous examples of allosteric control throughout biological systems, many of the mechanistic details have eluded scientists. A recent review of allosteric signal transduction highlighted the importance and simultaneous difficulty of elucidating the elaborate control mechanisms that are employed to regulate biochemical activity at a distal location from the chemical active site (*1*, *2*). Although each system has its own special requirements, universal components of allosteric regulation are defined by (i) a protein having at least two stereospecifically different receptor sites (an active site, which binds the substrate and completes a chemical reaction, and a distant allosteric site, which reversibly binds the allosteric effector) and (ii) the binding of the effector induces a reversible conformational transition in the protein that upregulates one or several of the kinetic parameters defining the biological activity of the protein.

A number of metabolic enzymes serve as excellent models of allosteric regulation, and in particular, the well-studied family of enzymes known as the glutamine amidotransferases (GATs)[1] provide an established framework for such studies. The GATs are remarkable molecular machines that have evolved to coordinate and synchronize the efficient production and subsequent incorporation of ammonia into a wide variety of metabolic substrates (*3*−*5*). However, despite a wealth of biochemical investigations, little is known about the precise details of the allosteric control mechanisms that afford GATs their exquisite, albeit complex, biochemical function.

The GAT family of enzymes share a number of common features. All are composed of (at least) a glutaminase domain and an acceptor domain. In the triad GAT subfamily, the glutaminase domain shares a common protein fold and a strictly conserved catalytic triad composed of a cysteine, histidine, and glutamic acid, which participate in the hydrolysis of glutamine to ammonia and glutamate. The acceptor domain varies in both the reaction it catalyzes as well as its fold. A particularly relevant feature of the triad GATs is the ability to upregulate their glutaminase activity upon binding of an allosteric effector at a remote binding site, although the degree of upregulation, the allosteric effector, and the allosteric site vary among the different enzymes (*6*−*9*). Without the acceptor domain, each indi-

† This work was supported by National Science Foundation grants MCB02-35144 and MCB04-46227, a National Resource Allocation Committee grant MCA03-50275 to Z.L.-S., and a National Institutes of Health grant RO1 GM067915 to V.J.D.

* Corresponding author. Phone: (217) 333-3518. Fax: (217) 244-3186

‡ Department of Chemistry, University of Illinois.

§ Department of Medicinal Chemistry & Molecular Pharmacology, Purdue University.

|| Present Address: Department of Chemistry & Biochemistry, University of California San Diego, La Jolla, CA 92093

⊥ Present Address: School of Pharmacy, University of Charleston, Charleston, WV 25304

# These authors contibuted equally to this work.

[1] Abbreviations: GAT, glutamine amidotransferase; IGP, imidazole glycerol phosphate; MD, molecular dynamics; NMA, normal mode analysis; PC, principal component analysis; PRFAR, N^1-[(5′-phosphoribulosyl)-formino]-5′-aminoimidazolecarboxamide ribonucleotide; SMD, steered molecular dynamics.

10.1021/bi061708e CCC: $37.00
Published on Web 01/30/2007

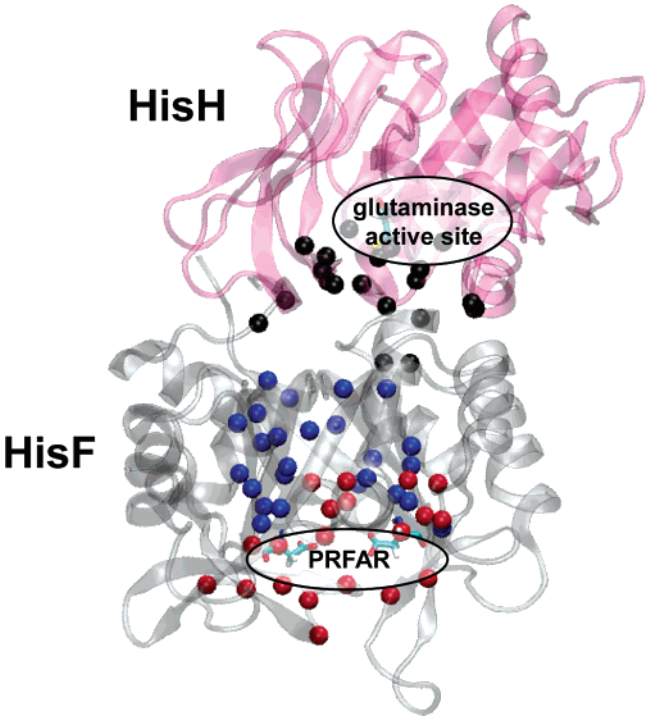

FIGURE 1: Allosteric pathways in IGP synthase. IGP synthase is shown in gray transparent cartoon, with residues involved in the allosteric pathway shown as solid spheres. A conserved network of interactions forms a signaling pathway that stretches from the PRFAR binding site shown in red on the C-terminus of hisF (PRFAR shown bound in licorice), up through the barrel shown in blue, across the interface shown in black, and into the glutaminse active site. The residues involved in allosteric regulation are marked in Supporting Information Figures 12 and 13.

vidual glutaminase domain has no activity (*10*). A third conserved feature is the channeling of the nascent ammonia product through the interior of the protein where it acts as a nucleophile in a subsequent reaction. The exact mechanism of ammonia transfer and the structural properties of each ammonia channel vary among the different enzymes. The "action-at-a-distance" upregulation of glutaminase activity makes the GATs a classic example of allosteric enzymes, and this common regulatory feature should not be surprising considering that maintaining cellular glutamine levels is an important feature for living organisms (*11*, *12*).

A particularly well-studied GAT is the enzyme regulating the fifth step of histidine biosynthesis, imidazole glycerol phosphate (IGP) synthase (Figure 1), which is composed of the glutaminase domain (hisH, a flavodoxin-like fold) and the cyclase domain (hisF, a $(\beta/\alpha)_8$ barrel). In IGP synthase, the allosteric effector of the glutaminase reaction is the unusual ribonucleotide N^1-[(5′-phosphoribulosyl)-formino]-5′-aminoimidazolecarboxamide ribonucleotide (PRFAR), which is the product of the previous step in the histidine pathway and also the substrate for the subsequent cyclase reaction. The bisphosphate ribonucleotide has an asymmetric architecture in which one side contains a glycerol chain moiety and the other a closed ribose ring. The cycle of events in IGP synthase begins with binding of glutamine in the glutaminase active site. Binding of PRFAR at the cyclase active site stimulates the hydrolysis of glutamine. The resulting ammonia then shuttles to PRFAR where the subsequent reaction, a carbon−nitrogen ligation and cyclization, takes place.

The three activities (glutamine hydrolysis, ammonia transfer, and synthesis of IGP) have been analyzed by a series of kinetic assays designed to measure the products of each reaction (Figure 2A). The glutaminase half-reaction activity is directly quantified by the oxidation of the glutamate product using a glutamate dehydrogenase-coupled assay. Ammonia transfer is deduced by measuring the stoichiometry of the reaction, i.e., how many equivalents of glutamine are hydrolyzed per PRFAR turnover. The formation of the histidine intermediate, IGP, is assessed by the degradation of the starting material (PRFAR) in the presence of glutamine (i.e., the cyclase half-reaction). In wild-type IGP synthase, the full reaction is fairly rapid ($k_{cat} = 7\ s^{-1}$), with both the glutamine hydrolysis and PRFAR turnover tightly coupled so that each ammonia molecule produced is subsequently incorporated into PRFAR in a 1:1 stoichiometry. In the absence of PRFAR, the two-domain complex performs basal glutamine hydrolysis at a rate of one turnover every 3 min, and comparison of the kinetic rates indicates that the stimulation of glutaminase activity is increased 4900-fold with PRFAR (Table 1).

For IGP synthase, the first suggestion of a mechanism of action for the allosteric signal was presented by the investigators who reported the crystal structure for the yeast isoform with a glutamine substrate analogue bound in the glutaminase active site and PRFAR docked in the cyclase active site (*13*). On the basis of comparisons of the crystal structures from the yeast organism with substrates (*14*) and the bacterial organism without substrates (*15*), the authors suggested that the reaction mechanism involved a hinge-opening and hinge-closing motion of the two domains. The difference between the so-called "open" or "relaxed" (R) state and the "closed" or "tight" (T) state was reported to be a 7° change in the orientation of residues at the interface of the glutaminase and the cyclase domains. This "breathing motion" at the interface as well as the movement of a flexible loop in the cyclase active site were both speculated to play a role in the regulation of enzymatic activity. Studies of the channeling of ammonia revealed that some conserved residues at the interface function to optimize ammonia transport by excluding water (*16*) and that conserved residues along the ammonia channel act as an ammonia relay during the conduction process (*17*).

In order to probe the roles of residues involved in the transmission of the allosteric signal, key residues were mutated. To assess the role of the conserved salt bridge formed by *h*K181 (*h* indicates from the glutaminase domain hisH) and *f*D98 (*f* indicates from the cyclase domain hisF) found adjacent to the glutaminase active site in allosteric signal transmission across the interface, a double alanine mutation was pursued (*18*). The kinetic assays of the double alanine mutation revealed that both the glutaminase stimulation and stoichiometry of the reaction were substantially reduced (Table 1), indicating a disruption in the competence of the allosteric signal and the ammonia transfer process. *h*N12, adjacent to the glutaminase active site, forms stabilizing hydrogen bonds with the side chain of *h*N15 and the *h*K181−*f*D98 salt bridge. The *h*N12A mutation reduced the PRFAR glutaminase stimulation compared to the wild-type stimulation to just 100-fold over the basal rate, and the stoichiometry increased to 8:1, indicating a disruption in the ammonia transfer process. A mutation of *f*T104, which forms

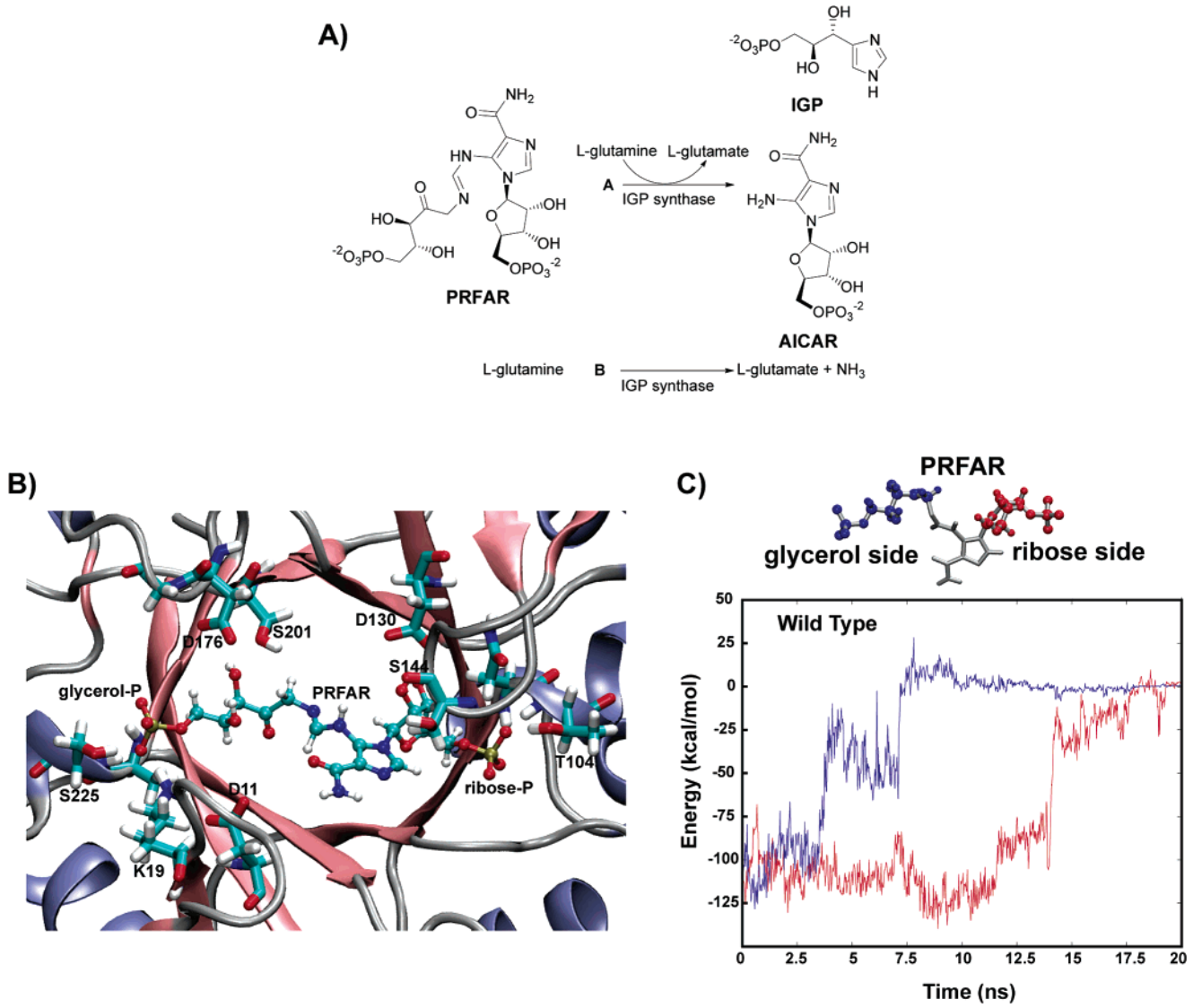

FIGURE 2: PRFAR interactions with the allosteric site. (A) Reaction A corresponds to the kinetic assay in which the concentration of PRFAR was varied and glutamine concentration was held constant (Table 1 cyclase and glutaminase half-reaction kinetic parameters). Reaction B corresponds to the basal activity glutaminase assay in the absence of PRFAR (Table 1 basal glutaminase kinetic parameters). (B) Snapshot of the glutaminase allosteric effector and cyclase substrate, PRFAR, bound in the active site of hisF, after a 6 ns equilibration. Conserved residues interacting with PRFAR are shown in licorice. Only connectivity between the atoms of PRFAR is shown; no double bonds are represented. Water molecules solvating the area and the glutaminase domain have been omitted for clarity. (C) The nonbonded interaction energies for the two sides of PRFAR are plotted as a function of time during the PRFAR undocking simulations. The glycerol side of PRFAR is presented in blue, and the ribose side of PRFAR is presented in red. Due to the high degree of symmetry within the substrate, the interaction energies for both sides of PRFAR were calculated between 21 PRFAR atoms (of similar type) and all residues of the cyclase domain within an 8 Å cutoff; therefore, differences in the energies are directly attributable to the varied interactions between each side and the residues in the surrounding cyclase active site. Water molecules solvating the area were not included in the energetic analysis.

a hydrogen bond to the ribose phosphate group at the C-terminus of β-strand 4, was found to reduce the allosteric signal upon PRFAR binding by 1000-fold. PRFAR turnover decreased by 760-fold, and the stoichiometry of the reaction increased to 3:1 (unpublished data, Table 1). Within the glycerol phosphate binding region, a conserved residue in the flexible loop, *f*K19, was also found to have a profound impact on the allosteric event. Although this residue is over 40 Å away from the glutaminase active site, mutation to alanine at this position reduced the allosteric stimulation 45-fold over basal levels (*13*). PRFAR turnover was again reduced 1000-fold, and the ammonia transfer process is measurably disrupted, exhibiting a 43:1 change in stoichiometry. Furthermore, equilibrium molecular dynamics (MD) simulations showed that mutation of the conserved *h*K181−*f*D98 salt bridge induced a structural destabilization within the glutaminase active site, as indicated by large dihedral fluctuations of the catalytic histidine ring (*18*). Although the kinetic assays were performed with the yeast isoform, the MD simulations were performed with the bacterial structure. A detailed comparison of the sequences and structures of the proteins established a high degree of homology between the two isoforms (Figures 7 and 8 in ref 16). Together, the complementary techniques suggested that the conserved salt bridge acts as a conduit of information between the two subunits (*18*).

The characterization of allosteric signals is challenging, as it requires the ability to monitor several residues at spatially distinct sites, as well as different time intervals. Here, we report explicit evidence toward the mechanism of

Table 1. Experimental Kinetic Assays[a]

glutaminase kinetic parameters—basal (no PRFAR present)				
mutation	K_m, basal[b] (mM)	k_{cat} (s^{-1})	k_{cat}/K_m (M^{-1} s^{-1})	k_{cat}/K_m WT/mutant
wild type	4.7 ± 0.2	$5.5 \pm 0.1 \times 10^{-3}$	1.18 ± 0.06	
N12A	2.3 ± 0.6	$1.4 \pm 0.1 \times 10^{-3}$	0.23 ± 0.06	5
K181A−D98A	1.6 ± 0.3	$3.0 \pm 1 \times 10^{-3}$	2.2 ± 0.8	0.5
T104A	2.0 ± 0.2	$2.0 \pm 0.2 \times 10^{-3}$	1.2 ± 0.2	1
K19A	2.7 ± 0.1	$8.1 \pm 0.5 \times 10^{-3}$	3.1 ± 0.2	0.4

glutaminase kinetic parameters—stimulated (with PRFAR present)					
mutation	K_m, half-reaction[c] (mM)	k_{cat} (s^{-1})	k_{cat}/K_m (M^{-1} s^{-1})	k_{cat}/K_M stimulated/basal	stoichiometry glutamate/IGP
wild type	1.2 ± 0.1	6.8 ± 0.2	$5.8 \pm 0.8 \times 10^{3}$	4900	1:1
N12A	5 ± 1	0.1 ± 0.03	23 ± 7	100	8:1
K181A−D98A	0.5 ± 0.04	0.209 ± 0.003	$3.9 \pm 0.3 \times 10^{2}$	180	110:1
T104A	1.4 ± 0.2	$6.0 \pm 0.4 \times 10^{-2}$	42.0 ± 8	35	3:1
K19A	1.2 ± 0.1	0.172 ± 0.005	$1.4 \pm 0.1 \times 10^{2}$	45	43:1

cyclase kinetic parameters				
mutation	K_m, Gln[c] (mM)	k_{cat} (s^{-1})	k_{cat}/K_m (M^{-1} s^{-1})	k_{cat}/K_m WT/mutant
wild type	1.8 ± 0.2	6.9 ± 0.3	$3.8 \pm 0.4 \times 10^{3}$	
N12A	4.8 ± 0.9	$1.9 \pm 0.02 \times 10^{-2}$	4.0 ± 0.8	950
K181A−D98A	2.3 ± 0.3	$7.0 \pm 2 \times 10^{-3}$	3.2 ± 0.9	1000
T104A	2.1 ± 0.2	$1.04 \pm 0.02 \times 10^{-2}$	5.0 ± 0.5	760
K19A	6.5 ± 0.5	$2.5 \pm 0.1 \times 10^{-2}$	3.6 ± 0.3	1000

[a] Data for wild type, N12A, K181A−D359A, and K19A were published previously in refs 13 and 18. [b] Glutamine hydrolysis in the absence of PRFAR. This corresponds to reaction B in Figure 2A. [c] Glutamine was the varied substrate, and the concentration of PRFAR was held constant at 100 μM. This corresponds to reaction A in Figure 2A.

allosteric regulation in IGP synthase. Principal component analysis (PCA) of the equilibrium MD trajectories and normal mode analysis (NMA) of the crystal structure indicate that the dominant principal components and low-energy protein vibrational modes could be involved in the transition from the open to closed states. In order to mimic the effects of effector binding, steered molecular dynamics (SMD) is employed to induce the unbinding of PRFAR from the cyclase active site. The application of SMD allows us to bridge several time and length scales, and the results highlight the promise of the technique for studying complex enzymatic reactions. An evolutionary analysis reveals a highly conserved network of interactions (Supporting Information Figures 12 and 13) leading from the PRFAR binding site, through the barrel, across the interface of the two domains, and into the glutaminase active site. An analysis of the correlated motion over the course of the allosteric transition further substantiates the role of the residues within the conserved network. Although many of the residues within the conserved network line the required ammonia channel, other residues not involved in the ammonia channeling event may be important for reliable transmission of the allosteric signal. Similar conserved allosteric networks have been found in other protein systems (*19*, *20*), but here, the evolutionarily conserved network is tested and probed in conjunction with molecular dynamics. Established experimental kinetic assays of the wild-type and mutant systems allow us to ascertain the function of various residues along this conserved communication pathway. Ultimately, we have discovered a range of large and small scale motions associated with transmission of the allosteric signal and thus are able to offer a model of allosteric regulation for IGP synthase that is consistent with several lines of experimental and theoretical data.

1. COMPUTATIONAL METHODS

1.1. Simulations. System Setup. The crystal structure used in all simulations is the *Thermotoga maritima* structure (1GPW). Chains C and D of the hisH−hisF complex were chosen because the flexible loop on the C-terminal end of hisF was resolved in a closed, active conformation. The orientation of the two domains for the T state was modeled after the *Saccharomyces cerevisiae* crystal structure, which was crystallized with PRFAR bound in the cyclase active site; in the yeast structure, the interface is reported to tighten by approximately 7°(*14*). Active-site residues in both subunits were analyzed according to available biochemical information. In the glutaminase active site, H178 of the catalytic triad is protonated on both its δ- and ϵ-nitrogens, the catalytic cysteine is deprotonated, and a free glutamine substrate was placed near the oxyanion hole; this scenario is consistent with a pre-reaction enzymatic state (*4*, *21*). For the synthase domain, hisF, the original crystal structure has an active-site mutation that was mutated back to its wild-type form (D11N). For the T-state simulations, the parametrization of the ribonucleotide substrate of hisF were performed using analogy following the established CHARMM protocol (*22*−*24*) and are briefly described in refs 25 and 26. All crystal waters were kept, and no additional water molecules were added to the interface. Hydrogens were added with PSFGEN, and explicit TIP3 water molecules were added as solvent with SOLVATE (*27*) through VMD (*28*).

The T- and R-state systems (which consisted of approximately 50 000 atoms each) were minimized for 10 000 steps and then equilibrated for 6 ns in the NPT ensemble using periodic boundary conditions with a flexible cell and the hybrid Nosé-Hoover Langevin piston method (*29*) to

control pressure at 1 atm. Particle Mesh Ewald was employed to efficiently treat electrostatics without a cutoff (*30*); the van der Waals cutoff was set to 12 Å with a switching function that started at 10 Å. Temperature was held constant at 298 K with Langevin dynamics. The time step for integration was 1 fs, and a multiple time-stepping algorithm was utilized, where bonded interactions were evaluated at every time step, short-range nonbonded interactions were evaluated every two time steps, and long-range electrostatics forces were evaluated every four time steps (*31*, *32*). All of the simulations including the SMD trajectories were performed with NAMD2 (*33*) using the CHARMM27 forcefield (*22*) and the TIP3 water model (*34*). Simulations were performed on the National Center for Supercomputing Application's (NCSA) Xeon Cluster (Tungsten) with 64 processors and a local Mac cluster (Turing). Each nanosecond of equilibration and SMD took approximately 10 h on each machine.

Two specific point mutations were introduced to the wild-type T-state system after the 6 ns equilibration. *f*T104 (T365 in yeast) of the cyclase domain was mutated to alanine, and the interdomain salt bridge formed by *h*K181 (K196 in yeast) and *f*D98 (D359 in yeast) was eliminated with the double alanine mutation, *h*K181A−*f*D98A. Each of the mutants were subject to a short minimization, followed by a 6 ns equilibration, before PRFAR undocking was inititated.

1.2. Steered Molecular Dynamics to Induce Substrate Undocking. Traditional MD simulations allow the exploration of biomolecular events; however, because of the typical 1 fs integration timesteps, they are generally limited to sampling events on the nanosecond time scale. Of course, many interesting and relevant biological processes occur on the order of microseconds to milliseconds and slower. Steered molecular dynamics (SMD) is an extension of traditional MD that applies external "steering forces" to biomolecular systems in order to accelerate otherwise prohibitively slow biological processes (*35*). It has been successfully applied to investigate a wide variety of biological events, including the unfolding of the cell adhesion protein fibronectin (*36*, *37*), the docking of cytochrome c2 to the reaction center (*38*), and stalk rotation in ATP synthase (*39*). Furthermore, SMD simulations have been combined with Jarzynski's identity (*40*, *41*) in order to reconstruct free energy profiles along relevant reaction coordinates from repeated pulling experiments. An extensive pedagogical discussion of the various SMD parameters and their impact on the reconstruction of free energy profiles can be found in ref 42. These techniques were used to investigate the energetics of ammonia conduction through IGP synthase (*17*) and again to demonstrate the preference of its hydrophobic $(\beta/\alpha)_8$ barrel to conduct ammonia over water (*16*).

In this work, constant-velocity SMD was applied to the system in order to remove PRFAR from the hisF active site. Physically, the new system Hamiltonian becomes $H[\underline{x}(t), t)] = H_0[\underline{x}(t)] + 0.5k[z(\underline{x}) - z_0 - \upsilon t]^2$, where $H_0[\underline{x}(t)]$ is the Hamiltonian of the initial equilibrated wild-type or mutant system with PRFAR bound, υ is the velocity of the harmonic constraint used to pull PRFAR, z_0 is the initial position of the center of mass of PRFAR, and $z(\underline{x})$ is the position of the center of mass of PRFAR at time t. For all simulations, we chose a harmonic constraint of $k = 500$ pN/Å.

Initially, we pulled the center of mass of PRFAR, in which the forces are distributed to all the atoms, along a direction perpendicular to the plane of the C-terminus of hisF at a speed of 5 Å/ns. It was clear from these initial SMD simulations that the phosphate groups formed the strongest interactions with hisF; thus, we modified the application of the forces so that forces were only applied on the two phosphate groups. Variations in the PRFAR pulling direction were examined, and as the sequence of PRFAR unbinding events were the same, we report only the downward pulling results. It is important to note that, regardless of the exact pulling direction, pulling speed, or choice of atoms for the applied force, the general behavior of PRFAR unbinding was the same among the various trajectories. Different pulling speeds and pulling vectors were tested for both the wild-type and T104A mutant system. The final set of simulations reported here applied SMD forces to only the two end phosphate groups in the direction perpendicular to the hisF C-terminus at a speed of 1 Å/ns. To prevent excessive translational motion of the protein during the SMD runs, two atoms far from the interface of hisH were held fixed (the C_α atoms of *h*R78 and *h*E150). Each PRFAR undocking run lasted 20 ns, and snapshots and interaction distances were extracted from these runs. A movie illustrating a representative PRFAR undocking trajectory is provided as Supporting Information online. In this movie, only hisH, hisF, and PRFAR are shown (water molecules are present in the simulation but are not displayed). The applied SMD forces are represented as green arrows, and the size of the arrows fluctuate corresponding to the forces applied at that time step.

1.3. Principal Component Analysis of the R and T States. Principal component analysis (PCA) of the motion of the α-carbon atoms during the equilibration of states R (without PRFAR) and T (with PRFAR) was performed as implemented in the statistics toolbox of MATLAB Release 13 package (The Mathworks, Natick, MA). PCA is a conventional method used to investigate the collective motion of residues in a protein (*43*−*47*) by evaluation of the covariance matrix **Cov**:

$$Cov_{ij} = \langle (r_i(t) - \langle r_i(t) \rangle)(r_j(t) - \langle r_j(t) \rangle) \rangle$$

where $\langle ... \rangle$ indicates a trajectory average and the coordinates of the α-carbon atoms at time t are denoted by the vector $\vec{r}(t) = [x_1(t)\ y_1(t)\ z_1(t)\ ...\ z_N(t)]^T$. If residues i and j do not have any correlated motion or if they vary rapidly, Cov_{ij} is close to zero. In PCA, the covariance matrix is diagonalized by solving the equation $\Lambda = \mathbf{T^T CovT}$ to obtain the diagonal matrix Λ, which contains the eigenvalues ranked by their magnitude. The largest eigenvalue and its accompanying eigenvector (contained in the first column of matrix **T**) correspond to the collective motion capturing the greatest fraction of observed variance in the protein. The covariance matrix was calculated over the entire trajectory after removal of initial transients.

In addition to the transformation matrix **T**, the contribution of each eigenvector T_i to the overall motion is obtained in the projection matrix P. Each column in the projection matrix represents the time evolution of the system in the principal component variables. The transformation matrix was used to convert between the projection in the principal components and the Cartesian coordinates using the equation

$$\Delta r(t) = r(t) - \langle r(t) \rangle = \mathbf{T}p(t)$$

where $p(t) = [p_1(t)\ p_2(t)\ ...\ p_{3N}(t)]^T$ is a vector of size $3N$, the i^{th} component being the projection along principal component i at time t . In order to determine the number of components n required to describe the full trajectory, the contribution of each eigenvector to the overall motion of the protein was calculated using the eigenvalue (Figure 3) of the corresponding principal component that is proportional to the mean square deviation of the protein due to its evolution along that principal component. In addition, on projecting the data from principal component i onto the Cartesian coordinates, the mean square deviation of each residue was calculated due to the i^{th} principal component (Figure 4). The mean square deviation (MSD) plots give an estimate of the flexible regions whose motion is highly coupled because of the i^{th} principal component.

During the undocking of PRFAR from hisF, the hisF−hisH interface opened up with the largest change in distance between interface residues occurring between *h*H53 and *f*Q118 (interface distance increases by 6.98 Å); the smallest change occurred between the conserved cation−π interaction formed by *h*W123 and *f*R249. The angle formed by the C_α atoms of *h*H53, *f*R249, and *f*Q118 was used as an order parameter to define the state of the system. The angle formed by the three residues was 22.1° in the crystal structure of the R state (chains C and D of 1GPW); it was 15.0° in the modeled structure for state T, indicating a difference of 7.1° between the two states. At the end of the SMD simulation, the angle increased by 12°, indicating the allosteric signal transmitted by the removal of the substrate PRFAR as well as a contribution from the nonequilibrium nature of SMD.

We have performed PCA of the hisF−hisH complex during equilibration in both the states to measure the differences in the motion of the complex due to the presence of PRFAR. The hisF−hisH complex has 453 residues, which implies 1359 degrees of freedom. Of these, the translational and rotational degrees of freedom are removed by aligning the center of mass of the α-carbon atoms to the initial frame using VMD; in addition, the C_α atoms of two residues of hisH are held fixed during SMD. We have 4.955 ns of trajectory for the complex with PRFAR bound, and frames are recorded every 0.5 ps yielding 9910 frames for this state. In the case of the hisF−hisH complex in the open state, 5.1 ns of simulation was obtained yielding 10 200 frames.

1.4. Analysis of MD Trajectories. A variety of tools was used to analyze the trajectories. The majority of the energetic analyses were performed with the freely available MDEnergy trajectory energy analysis tool, which is now available as a plugin in VMD (*28*). The nonbonded energies between the two PRFAR moieties and all cyclase residues within 8 Å of each group are presented in Figure 2C and were calculated using MDEnergy with the CHARMM27 forcefield, a dielectric constant of two for the electrostatic calculations, a van der Waals cutoff of 12 Å, and a switching function that begins at 10 Å. The electrostatic potential maps presented in Supporting Information Figure 14 were computed with the PME plugin in VMD 1.8.3. Separate PDB and PSF files for hisA (1q02.pdb) and hisF (1gpw.pdb, chain A) were created with the CHARMM27 force field, and a pad of 15 Å was used to calculate the potentials.

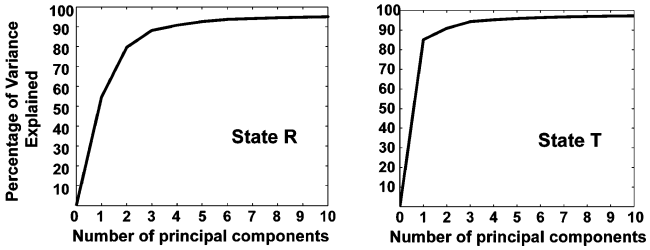

FIGURE 3: Contribution of principal components to motion of complex. The contribution of the principal components to the variance in the motion of the protein complex during the trajectory for state R and state T is shown.

Structural analyses of the trajectories was performed with handwritten scripts and Multiple Alignment (*48*), a VMD 1.8.3 plugin. The various structural alignments reported here used a modified version of STAMP that is incorporated into the Multiple Alignment plugin (*49*). To evaluate the structural variation in the IGP synthase structure throughout the pulling simulations, various snapshots were aligned using the STAMP algorithm and then evaluated according to Q, a measure of structural homology developed by Wolynes and co-workers (*50*). Q is evaluated according to the following equation: $Q = (2/(N-1)(N-2))\Sigma_{i<j-1}\exp[-((r_{ij} - r_{ij}^{eq})^2/2\sigma_{ij}^2)]$ where r_{ij}^{eq} is the $C_\alpha - C_\alpha$ distance between residues i and j in the equilibrated structure. A Q value of zero implies no homology; a Q value of one means the structures superimpose perfectly. This dynamic structural analysis allowed us to ascertain which regions of the protein were changing throughout the PRFAR undocking simulations.

1.5. Correlation Analysis of SMD Trajectory. Correlations between the residues in the protein complex were analyzed in a 20 ns SMD trajectory in which the allostric effector PRFAR was undocked. The energetic analysis of the PRFAR undocking trajectory indicated a series of rupture events (Figure 2C); this was used to break up the SMD trajectory into five segments: 0−3.3 ns (segment 1), 3.3−6.2 ns (segment 2), 6.2−7.2 ns (segment 3), 7.2−9 ns (segment 4), and 9−19 ns (segment 5). The complex is in the R state at the end of 19 ns, and the time interval beyond 19 ns was discarded for this analysis, as PRFAR is completely undocked by that time.

We define the correlation between the i^{th} residue and the j^{th} residue as

$$C_{ij}(T) = (\langle \Delta\vec{r}_i(t)\Delta\vec{r}_j(t)\rangle / (\langle \Delta\vec{r}_i(t)^2\rangle\langle \Delta\vec{r}_j(t)^2\rangle)^{1/2})$$

where $\Delta\vec{r}_i(t) = \vec{r}_i(t) - \vec{r}_i(t - \Delta t)$, $\vec{r}_i(t)$ is the position vector of the C_α atom of the i^{th} residue of the proteins hisF or hisH or the phosphorus (P) atom of PRFAR at time t, and $\langle ... \rangle$ refers to the time average over time interval T. This correlation matrix is qualitatively similar to the dynamic cross correlation matrix (DCCM), which has been used to characterize the correlation in motion of protein residues (*47*, *51*−*53*) but is quantitatively much stricter than DCCM (results not shown). If the residues move in the same direction in most of the frames, the motion is considered to be correlated and $C_{ij}(t)$ will be positive; if they move in opposite directions in most frames, the motion is said to be anticorrelated and $C_{ij}(t)$ will be negative. If the motion between the two residues is close to zero, then the motion is said to be uncorrelated. If the two residues move in

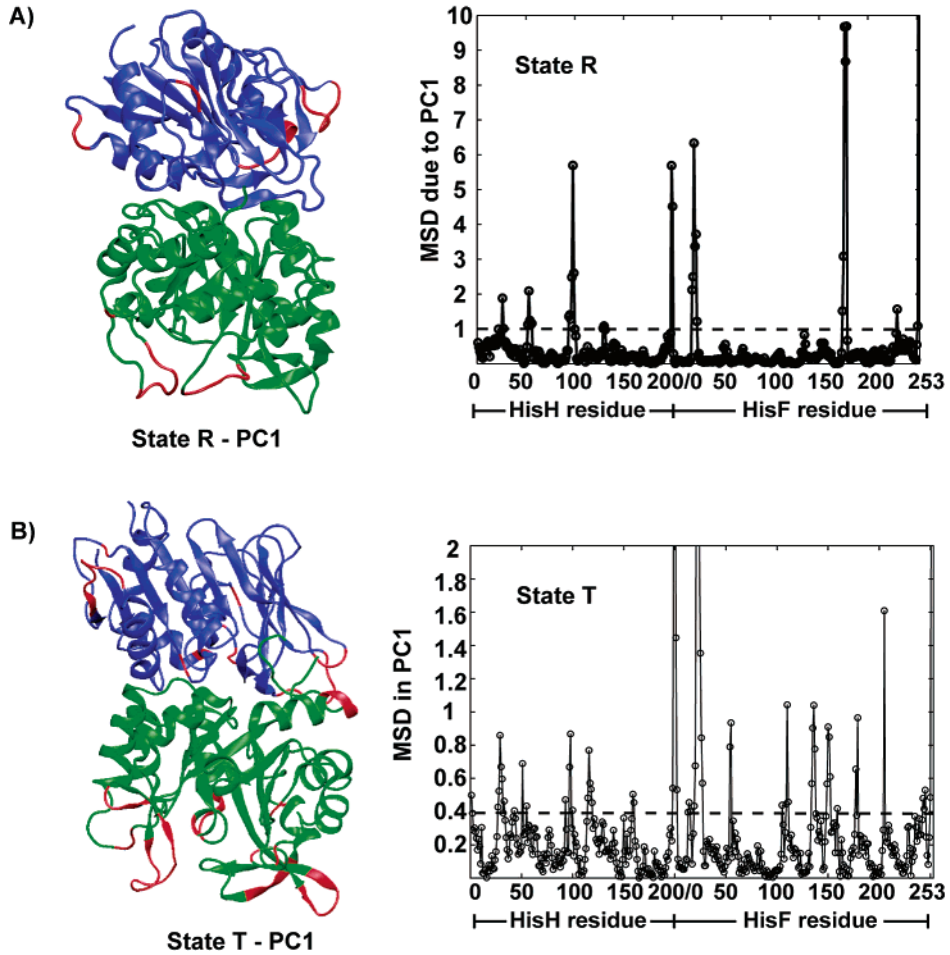

FIGURE 4: Dominant motion in PCA. The protein complex hisF−hisH is shown in secondary structure. HisF is colored green, and hisH is colored blue. The MSD per residue and the residues with high MSD in PC1 (A) in state R (without PRFAR) (MSD ≥ 1) and (B) in state T (with PRFAR) (MSD ≥ 0.4) are shown in red.

perpendicular directions in a correlated fashion, its correlation value will also be close to zero and is an artifact of this correlation function. The frames are saved at an interval of every $\Delta t = 0.5$ ps, and a total of 38 000 frames were analyzed for the correlation matrices.

2. RESULTS

2.1. Principal Component Analysis of R- and T-State Simulations. Protein dynamics are often dominated by large-scale collective motions involving large parts of the structure. A well-established method used to investigate these collective motions is principal component analysis (PCA) of molecular dynamics simulations. PCA has been used to decompose dynamics as well as to search for coupled motion leading to conformational changes (*43*−*45*, *47*). The method can also be used to reduce the phase space of an MD trajectory by projecting its motion along the principal component variables, which usually requires only a few components to approximate the full trajectory.

In this work, PCA is employed to capture the most significant principal components of the motion exhibited by the hisF−hisH complex both in the T state (tight, PRFAR bound) and R state (relaxed, no PRFAR bound). The difference in the collective motions between the two states are directly attributable to the presence (or absence) of PRFAR. Because it has been experimentally determined that the allosteric signal is propagated upon PRFAR binding, inspecting the inherent differences in the dominant motions between the two enzymatic states is a relevant step toward understanding the allosteric signal. The differences in the motion between the two enzyme states are quantified by the PCA, and these differences are interpreted in light of how they would affect or alter the competency of the allosteric signal. The dynamics of the protein complex due to the individual principal components can be visualized by projecting the motion due to these components onto the structure. In addition, the motion due to the first two components (PC1 and PC2) can be further analyzed by measuring the MSD of each residue due to the respective modes. For both states, this analysis indicates that the most flexible regions in the complex are the loops at the hisF active site.

In the R state, the protein exhibits large motions in the region of the flexible loops that close upon PRFAR in the T state. As shown in Figure 3A, 55% of the motion in the R state can be described in terms of PC1 and an additional 25% of the motion is described by PC2. The third principal component (PC3) accounts for only 9% of the variance, and the amount of motion explained by additional principal components reduces further. The motion due to the first two PCs will be used as an approximation to study the overall dynamics of the protein complex in the R state.

Without PRFAR bound in the hisF active site, the dominant motion in PC1 couples the motion of the loops in

the hisF active site to loops in the hisH domain (Figure 4). The large motion of the flexible loops within the hisF active site is not surprising because PRFAR is not present to contribute stabilizing interactions (hydrogen bonds and salt bridges between residues in the flexible loops and PRFAR). The MSD of the residues at the interface as it tightens is less than that of the residues at the active site, indicating a weak coupling between the motion in the hisF active site and the interface breathing motion when PRFAR is not bound. PC1 couples the motion of residues 20 to 25, 174 to 178, and 230 in the active site of hisF to that of residues 52−56 and 94−99 at the interface of hisH. In addition, residues 129, 130, 26, and 27 from hisH were shown to be coupled to the motion at the interface in PC1. PC2 corresponds to large movements in the hisF active-site loops and small motions in hisH strand 5 and the loop following helix 4 and strand 5, composed of residues 98−101 and 111−119 (Supporting Information Figure 15). Moreover, PC2 does not indicate any perceivable motion at the interface.

In the T state, the MSD for each residue indicates that the amount of motion in this state is much smaller than that in the R state. The large RMSD of N- and C-termini are artifacts of PCA and is comparable in the two states. The major motions coupled in PC1 are the breathing motion at the interface (characterized by movement of residues 51, 98, and 114 to 118 of hisH) with the motion of the loops within the hisF active site (interacting with PRFAR). A collective analysis of PC1 indicates that a slight opening (or breathing) motion at the interface is coupled to the closing of the loops around PRFAR. Moreover, the MSD due to the motion at the interface is comparable to the closing motion of the loops around the active site in state T. The dominant motions in PC2 further substantiate the coupling of the motion at the interface (residues 94−97 of hisH) with the loop motion within the hisF active site (Supporting Information Figure 15). In the R-state simulation, the interface closes by 2.2° where, as in the T-state simulation, the interface opens by 1.1°.

2.2. Steered Molecular Dynamics of PRFAR Undocking. General Features of PRFAR Recognition. PRFAR docks to the C-terminus of the cyclase domain through the formation of several nonbonded interactions with conserved phosphate binding site residues. Although the majority of these interactions are hydrogen bonds to backbone amide groups, some conserved side-chain hydroxyl groups and salt bridges also participate in PRFAR binding (Figure 2B). The bisphosphate ribonucleotide has an asymmetric architecture in which one side contains a glycerol chain moiety and the other a closed ribose ring. The two phosphorus atoms in PRFAR are designated as glycerol phosphate (gP) and ribose phosphate (rP) depending on the side of PRFAR to which they belong. As evidenced by the energetic interactions at the beginning of the SMD undocking trajectory, shown in Figure 2C, the two sides of PRFAR display different affinities for the cyclase active site, with the ribose side being more tightly held.

Over the course of the wild-type undocking trajectory, the correlated motion between the substrate PRFAR and the protein (Figure 5) is measured over the five time segments, as determined by the trajectory (see methods). In this analysis, the protein residues having a correlation value >0.05 are considered to be highly correlated to the substrate. It should be noted that two residues in hisH were held fixed in the SMD simulations, and as a result, the correlation of hisH residues with the substrate is dampened. In fact, none of the residues in hisH were found to be highly correlated with the substrate during the undocking trajectory. Over all the time domains, the residues with the highest degree of correlation to the substrate are either conserved or are the nearest neighbors in sequence of these conserved residues. This result implies that conserved residues make the most important contributions to substrate recognition and that residues in their vicinity are highly correlated to PRFAR through backbone interactions.

The undocking behavior was examined using different PRFAR pulling directions and velocities in several simulations. A comparative analysis of the PRFAR undocking dynamics in the various trajectories indicated that, regardless of the pulling speed (either 5, 3, or 1 Å/ns) or pulling angle, the general features of PRFAR unbinding were the same. To probe the effect of mutations on the PRFAR unbinding dynamics, we also simulated PRFAR undocking from the two mutant systems, *h*K181A−*f*D98A and *f*T104A, at the slowest pulling speed.

In general, many of the features of the PRFAR undocking trajectories in the wild-type and mutant systems are the same. Most notably, the gP moiety of PRFAR always undocks first, followed by the rP moiety. Within the gP side, *f*K19 always makes a long-lasting salt bridge with the phosphate group, and catalytic residue *f*D11 makes hydrogen bond contacts to the glycerol chain hydroxyl groups during undocking. On the rP side, long-lasting hydrogen bonds between *f*D130 and the ribose hydroxyl groups are also a common feature. The flexible loops at the hisF active site allow for some inherent variability in local motions. In *f*T104A, loss of the *f*T104 hydrogen bond at the ribose side allows more motion of PRFAR initially, leading to the formation of a salt bridge between K179 and the glycerol phosphate during the minimization. Although changes in salt bridge partners do change the time at which the glycerol side detaches (data not shown), the general sequence of events is left unchanged.

As the SMD force is applied, the first contacts to break occur at 3.3 ns, when the hydrogen bond between gP and *f*A224 ruptures. At 3.8 ns, the hydrogen bond with the hydroxyl group of *f*S225 is broken. The long residence time of this hydrogen bond is reflected by the high degree of correlation for both of these residues with gP in the first time segment, with this correlation being lost in subsequent time segments (Figure 5). The catalytic aspartate *f*D11 forms a hydrogen bond with a hydroxyl group of the glycerol moiety, and it remains correlated to gP throughout the first two time segments. Although PRFAR is being pulled out of the active site, the gP maintains salt bridges with *f*K179 and *f*K19 located on the flexible loop, causing both lysines to be drawn outside of the active site, until the contacts break at 6.2 and 7.2 ns, respectively. *f*K19 plays an important role in PRFAR recognition, as it remains correlated to gP over the first three time segments and is the most persistent contact from the initial binding site of gP. Once the salt bridge is broken, *f*K19 shifts back into the active site to form a salt bridge with *f*D11. At this point, the glycerol chain hydroxyl groups form transient hydrogen bonds with conserved *f*D176. *f*S144, residing in the loop between *fβ*5−*fα*5, forms a hydrogen bond with the aminoimidazole carboxamide group

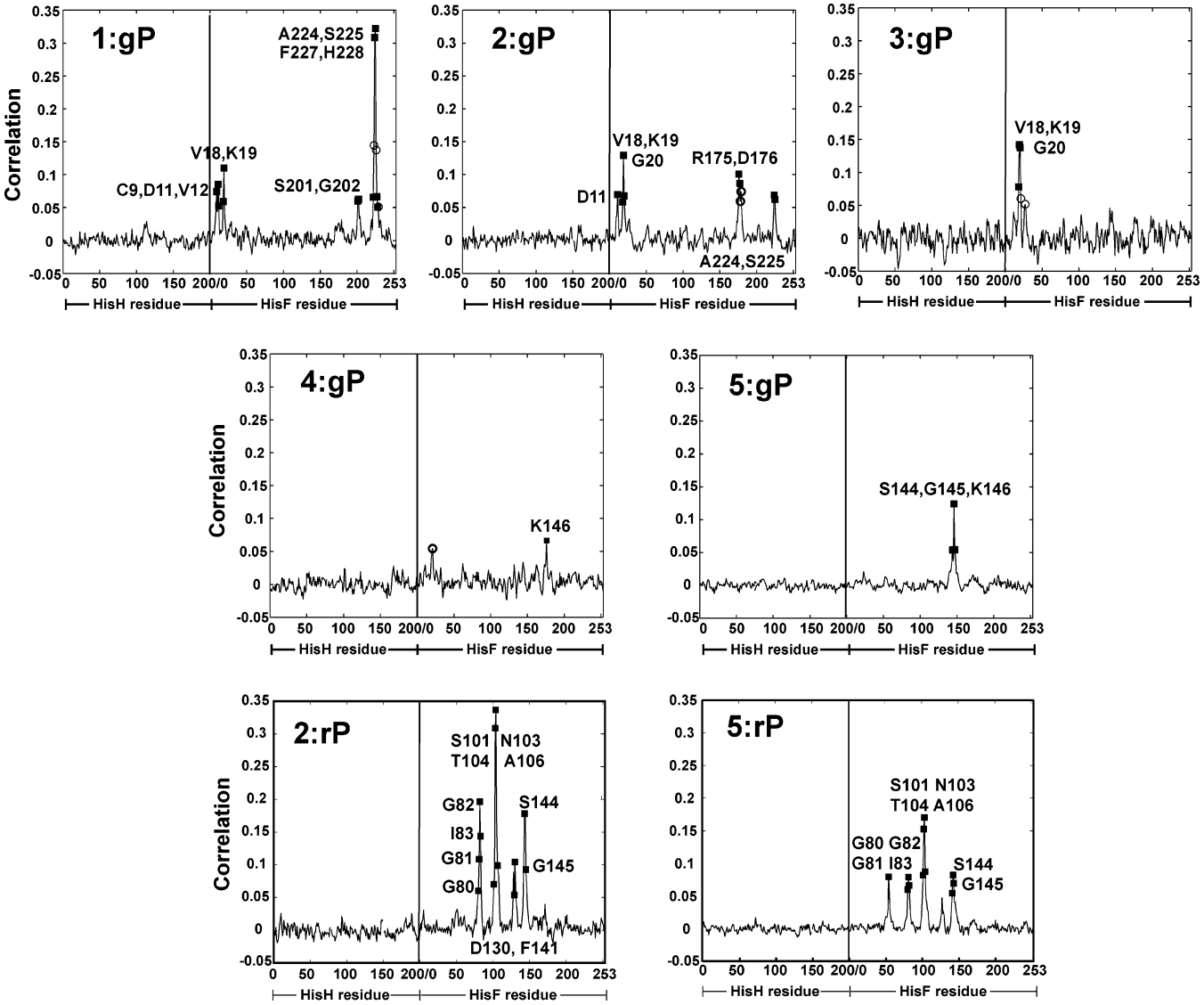

FIGURE 5: Correlations of substrate undocking to protein motions. The correlation in motion of the residues of the protein complex to the P atoms in the glycerol side (gP) of PRFAR for time segments 1−5 and in the ribose side (rP) for segments 1 and 5. Conserved residues are shown as filled squares and marked; the unconserved residues are shown as open circles.

on PRFAR at 9.2 ns. At 9.3 ns, the gP group forms a salt bridge with *f*K146; this salt bridge is maintained throughout the rest of the PRFAR undocking simulation and forms the last contact to break before PRFAR is completely removed from the active site (around 19 ns), remaining correlated throughout segments 4 and 5.

Initially, when PRFAR is docked, residues *f*G81, *f*G82, and *f*I83 make backbone interactions with the rP. In addition, the side chain of *f*D130 forms a hydrogen bond with one of the hydroxyl groups in the ribose of PRFAR. These residues are correlated to rP through all the five time segments. At 11.8 ns, the hydrogen bonds between the ribose hydroxyl groups and *f*D130 are broken and this initiates the first marked movement of the ribosyl side of PRFAR. At the same time, the hydrogen bond between the hydroxyl group of *f*T104 and the ribose phosphate group lengthens to 2.9 Å. At 14.1 ns, *f*S144 makes a transient hydrogen bond with one of the hydroxyl groups of PRFAR. The correlation of these residues to the rP remains strong through all five time segments, and most of the residues except *f*S144 and *f*G145 exhibit reduced correlation toward the end of the 20 ns trajectory. This shift in correlated motion indicates that the interactions of hisF with rP are stronger and more long-lasting than those with gP in the trajectory. The last contacts to PRFAR are made with residues in the loops between *fβ*2−*f*α2 and *β*5−α5.

2.3. Correlation Among Residues within the Barrel. The above correlation analysis indicates that residues having correlated motion with the substrate are either conserved or proximal to conserved residues. As PRFAR is pulled away from the hisF−hisH complex, the interface opens and the residues interacting with the glycerol side of PRFAR in the *β*-barrel exhibit a net downward displacement. Initially, gP interacts strongly with the loops following strands 1, 7, and 8 of the barrel, but these interactions are lost as the simulation progresses and PRFAR is removed. The allosteric signal is transmitted from the side of the barrel interacting with the ribose moiety of PRFAR (strands 3, 4, and 5) in the second half of the simulation, and hence, there must be some correlation between regions far off in sequence space during this stage of the simulation. To test whether conservation is an important factor for this network of interactions between

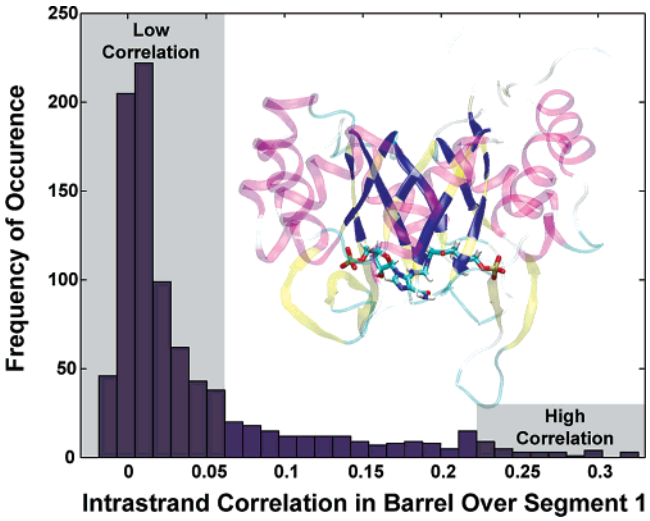

FIGURE 6: Histogram analysis of correlated motion in protein. Histogram of the correlation values for all pairs of residues from different strands of the barrel during time segment 1. Conserved residues with high correlation (C_{ij} > 0.23) are shown in blue on the protein.

residues within the barrel, the correlations between all pairs of residues found in the strands of the barrel were plotted as a histogram (Figure 6). In this analysis, only those pairs of residues are considered in which the residues belong to two different strands so that the backbone contribution to the correlated motions are neglected. The correlation values of the residues in the barrel are higher in general because the strands are in contact with each other through backbone hydrogen bonds. There are only 23 pairs of residues such that $C_{ij} \geq 0.23$, of which 15 pairs have both residues conserved, 5 pairs have only one residue conserved, and only 3 highly correlated pairs are formed by unconserved residues (Figure 6). These unconserved pairs, however, are the nearest sequence neighbors of highly conserved correlated pairs. Similar trends are also followed in the other time domains, which strongly suggests that conservation is a good indicator of correlated motion and an important component of allosteric signal transduction across the barrel.

Of the 41 residues present in the strands, 29 residues are conserved across all three domains of life with strands 1, 6, and 7 being completely conserved. In contrast, in hisA, which is homologous to hisF but exhibits no allosteric effect, only 16 of the 47 residues belonging in the barrel strands are conserved. The majority of the conserved residues in hisA reside on the C-terminus end of the barrel and are likely conserved for interactions with the substrate and catalytic purposes (data not shown). Two additional enzymatic features that are lacking in hisA include ammonia channeling and the allosteric effect, putting additional evolutionary constraints on hisF to conserve certain residues within the barrel.

2.4. Interface Motion during Undocking Simulations. Quantitative differences occur in the protein motion among the wild-type and mutant systems during the PRFAR undocking. The structural changes within the protein were monitored by structurally aligning snapshots extracted from the trajectories, followed by a *Q*-analysis and monitoring of the overall root mean square deviation (rmsd) (see methods). Interdomain distances were monitored at several locations across the interface between the following conserved residues: *h*K181 and *f*D98 (both $C_\alpha - C_\alpha$ and $N_z - O_{\delta 2}$ distances), *h*G52$-C_\alpha$ and *f*F120$-$C, *h*N15$-N_{\delta 2}$ and *h*K181$-N_z$, *h*N15$-N_{\delta 2}$ and *f*D98$-O_{\delta 2}$, *h*W123$-C_{\epsilon 2}$ and *f*R249$-N_\epsilon$, *h*R117$-C_\alpha$ and *f*T195$-C_\alpha$, and *h*N12$-C_\alpha$ and *f*L94$-C_\alpha$. Correlated motion for the wild-type simulation is reported and discussed below.

Wild Type. The wild-type simulation of the bacterial system showed the most significant and marked increase in interdomain distances at the interface during the PRFAR undocking simulations (Figure 7). This breathing motion is localized to the region of the interface between α-helices 1 and 2 of the glutaminase domain (hereafter referred to as *h*α1 and *h*α2, etc.) and *f*α3 and *f*α4 of the cyclase domain as labeled in Figure 9c. Two hydrogen bonds between *h*G52 and *f*F120 and *h*N12 and *f*L94 are initially in close contact, but their interaction distance systematically lengthens during the PRFAR pulling simulations. The *h*G52$-$*f*F120 interdomain distance increases from 4.39 Å to a maximum distance of 10.01 Å, and the *h*N12$-$*f*L94 interaction increases from an initial distance of 4.07 Å to a maximum distance of 10.15 Å. *h*G52 exhibits correlated motion with conserved residues *h*G11, *h*C84, *h*G86, *h*S142, and *f*G121 (Figure 8C,D). These residues are in close proximity to *h*G52 but do not have strong interactions with it. In the fifth time segment, which corresponds to the approximate R state, the interface opens up and the correlation between *h*G52 and *f*G121 is reduced; in addition, *h*G52 becomes more strongly correlated to *h*G11, as the backbone interaction has increased. Similar qualitative results are also obtained for the correlation of *h*N12 in the first and last time segments as seen in Supporting Information Figure 16. The interface opening motion in the simulations occurs mainly on the side of the barrel that interacts with glycerol (strands 1,7, and 8); this is likely because there are weaker interactions between hisH and hisF at the interface in this region as compared to the side of the barrel that interacts with ribose.

A network of salt bridge and hydrogen bond interdomain interactions are formed in the wild-type structure between *h*K181, *h*N15, and *f*D98, which are directly adjacent to the glutaminase active site. This network remains intact throughout the entire PRFAR undocking simulations (Figure 7) despite interface-opening motions occurring in a nearby region. The small degree of structural variation in the *h*K181$-$*f*D98 region is shown in Figure 7B. A time-dependent correlation analysis between the motion of *h*K181 and all other residues in the protein complex (Figure 8A,B) indicates that *h*K181 is highly correlated to *f*D98 as well as *f*P76. *f*P76 forms a backbone hydrogen bond with the side chain of *h*K181 and lines the entrance of ammonia into the mouth of the $(\beta/\alpha)_8$ barrel (*16*). In addition, *h*K181 is also correlated to conserved residues *h*N16 and *h*Y138. *h*N16 forms a hydrogen bond with *f*D98, and *h*Y138 forms a backbone hydrogen bond with the completely conserved *h*S182. The conserved salt bridge remains intact throughout the simulation, as seen by their high correlation over all five time segments.

Similarly, the conserved interdomain contacts at the hinge region of the interface, formed by a cation$-\pi$ pair between *h*W123 and *f*R249, also remain in a close and stable configuration throughout the undocking trajectory. The interdomain region between the C_α of *h*R117 in the glutaminase domain and the C_α of *f*T195 in the cyclase domain was

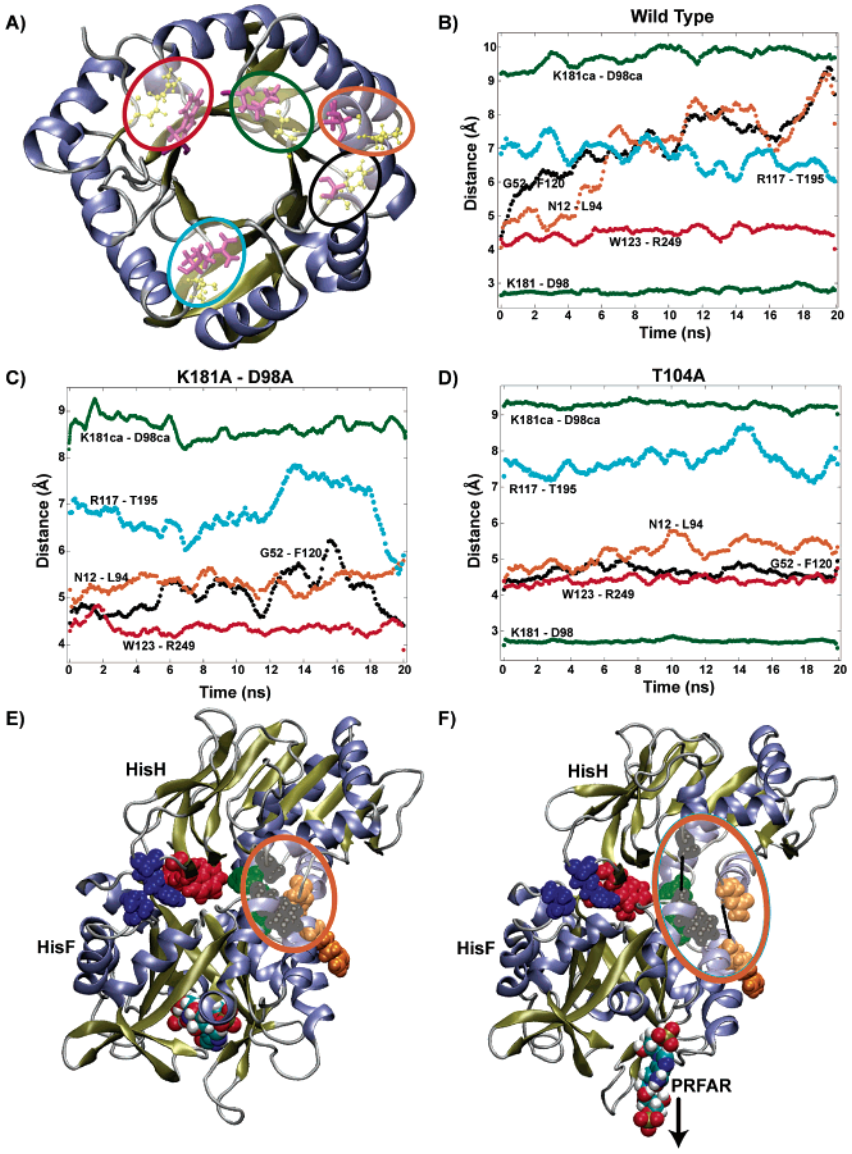

FIGURE 7: Interdomain distances throughout PRFAR undocking. Comparison of interdomain distances during the various PRFAR undocking simulations. (A) View of N-terminus of the acceptor domain (hisF) from the glutaminase active site. Regions of monitored interdomain distances are color-coded and highlighted. Interdomain distances for selected contacts are reported over the 20 ns pulling simulations for wild type (B), K181A-D98A (C), and T104A (D). Line colors correspond to regions colored in (A): G52−F120 interdomain distance depicted in black, K181−D98 depicted in green, R117-T195 in cyan, W123−R249 in red and N112-L194 in orange. (E) Wild-type IGP synthase shown at beginning of PRFAR undocking simulation. PRFAR shown as space-filling model in the hisF active site. Interdomain contacts, also shown as space-filling, correspond to the same coloring as in (A)−(D). (F) Same as (E), but at the end of the PRFAR undocking simulation. The hinge-opening motion is highlighed inside the orange ellipse for contact G52−F120.

also monitored; this distance was initially 6.23 Å and at the end of the simulation was 5.76 Å, indicating that this region was also stable. Similar quantitative results of the correlation analysis can also be observed for the cation−π interaction, as shown in Supporting Information Figure 16.

The overall structural changes accompanying the SMD driven allosteric transition can be seen in Figure 9C, which aligns a typical snapshot of the protein from the beginning of the pulling simulation with one from the end. The hinge-opening region is clearly visible. These results are consistent with suggestions from previous work that this region of the complex is subject to breathing motions that allow the entrance and exit of the glutaminase substrate (*18*). X-ray crystal structures of the yeast and *T. maritima* isoforms (*14*, *15*) also indicate a structural difference in this region. In addition, during the PRFAR undocking simulations, bulk water molecules rush into the hinge-open region of the interface, and a nearly complete exchange of the crystallographic waters is seen. This is in striking contrast to equilibrium MD simulations of the hinge-closed complex, which does not allow virtually any exchange of interface waters within the protected ammonia chamber formed at the interface (*16*). In a further SMD simulation, we saw that the glutamine could be easily removed from the interface of the open structure (unpublished results).

hK181A−fD98A. In this double mutant, the loss of the salt bridge at the interface greatly affects the interface opening dynamics. With loss of this interdomain contact, there is no longer a directed opening and closing hinge motion (Figure 7). Instead, the two subunits wobble about their respective positions. Initially, the active-site architecture of the glutaminase domain is slightly altered: the side chain of *h*N15, which in the wild type forms hydrogen bonds with the charged side chains of both *h*K181 and *f*D98, is instead

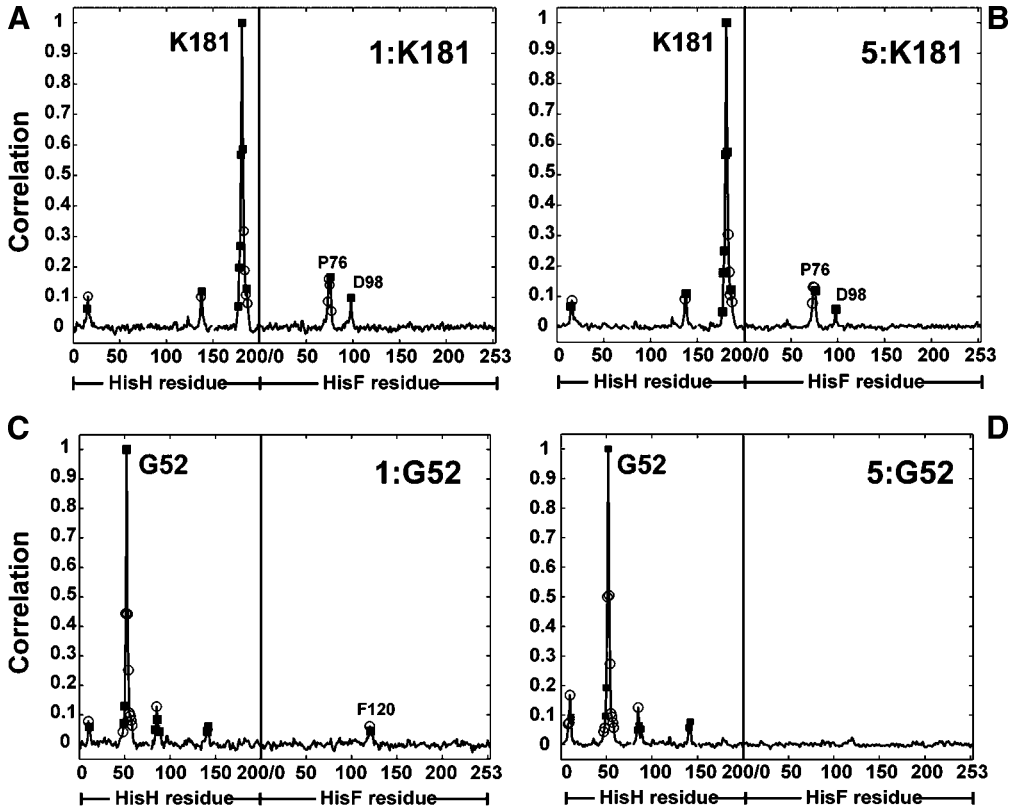

FIGURE 8: Correlation at the interface. Correlation of the conserved residues *h*K181 in time segment 1 (A) and time segment 5 (B) and *h*G52 in time segment 1 (C) and time segment 5 (D) are shown. *h*K181 forms a salt bridge with *f*D98, and this interaction remains correlated throughout the simulation; *h*G52 forms a hydrogen bond with *f*F120, which becomes weaker as PRFAR is undocked.

drawn outward, forming a hydrogen bond with the backbone carbonyl of strictly conserved *f*G96. The rearrangement near the glutaminase active site and the accompanying increase in the basal glutaminase rate is discussed in ref 18.

During the PRFAR undocking simulations, the dynamics of the cation−π pair (*h*W123−*f*R249) are unaffected from wild type (Figure 7C). The interdomain distance between the C_α of *h*R117 and the C_α of *f*T195 exhibited larger fluctuations, indicating a "wobble" motion in this area that is not seen in the wild type. The $C_\alpha-C_\alpha$ distance between *h*K181A−*f*D98A is also similar to the wild type, although the interdomain distance decreases because of the local structural rearrangement near the glutaminase active site. It is clear from the rmsd fluctuations as seen in Figure 9A that motion in the glutaminase domain is uncoupled from motion in hisF. Although there was significant motion in the cyclase flexible loops *f*β1−*f*α1 (residues 14−30) and *f*β5−*f*α5 (residues 136−152) accompanying the undocking of PRFAR, it did not induce a corresponding motion in the glutaminase domain, as was seen in the wild type. There is general wobbling in the interface in the *h*K181A−*f*D98A mutant, which allows for exchange of water, albeit not to the extent seen upon opening in the wild-type simulations.

fT104A. The dynamics at the interface and within the glutaminase subunit are different from that of the wild type, as reflected by the fluctuations in the contact distances (Figure 7D). Interestingly, although the *h*K181−*f*D98 interdomain salt bridge maintained approximately the same values on average, this contact showed less fluctuation as compared to both the wild-type and *h*K181A−*f*D98A mutant simulations. Within the cyclase domain, *f*D98 and *f*T104 are connected via the *f*β4 strand, and the hydroxyl group of *f*T104 interacts directly with the ribose phosphate group of PRFAR. Therefore, removal of the *f*T104 hydroxyl group results in a general decoupling of this strand to the PRFAR undocking, and an overall decrease in the motion of *f*D98 and its salt bridge contact to *h*K181.

Similar to the *h*K181A−*f*D98A mutant, the *f*T104A system did not exhibit a systematic increase in the interdomain contacts in the region near *h*α1, *h*α2, *f*α3, and *f*α4, indicating that removal of the T104 hydroxyl group impairs the correlated breathing motion at the interface. The *h*G52−*f*F120 interdomain contact is especially decoupled, exhibiting reduced fluctuations and little change in the overall interaction distance. However, the *f*T104A mutant exhibited a systematic increase in general cyclase domain motion, as compared to wild type. The loss of the *f*T104 hydroxyl group changed the PRFAR undocking dynamics such that the substrate interacted more with *f*β1, *f*β2, and the flexible loop residing between *f*β1 and *f*α1. It is clear from the simulations that this altered PRFAR motion caused an increase in the average rmsd for this region of the protein (upward of 12 Å), as illustrated in Figure 9A.

During the undocking trajectory with the *f*T104A simulation, there is less exchange of water at the interface than during the undocking simulation with the wild-type protein. This further indicates the complete uncoupling of the hinge-opening motion at the interface from the PRFAR unbinding event in the *f*T104A mutant.

2.5. Dynamics of the Flexible Loop. Loop "switching" on the C-terminus of $(\beta/\alpha)_8$ barrels is a common functional control motif. In the cyclase domain, the loop between *f*β1 and *f*α1 has been shown to be a dynamic, flexible loop and has been crystallized in both the open and closed conforma-

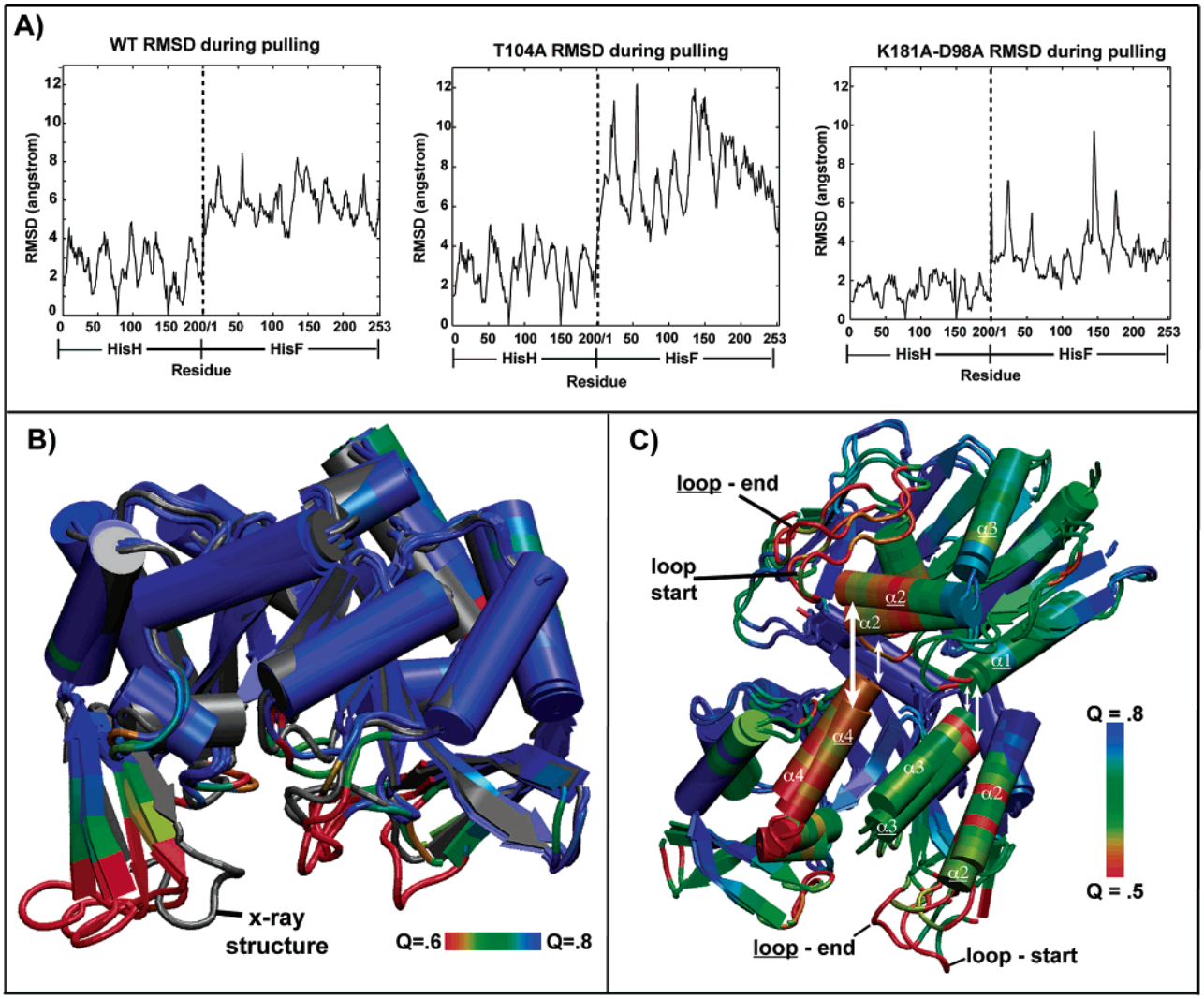

FIGURE 9: Comparisons of motion throughout PRFAR undocking. (A) Comparison of average rmsd per residue for the ligand unbinding simulations. C_α rmsd averaged over length of 20 ns pulling simulation for the wild type, T104A mutant, and K181A−D98A mutant. (B) The most open flexible loop conformations from each of the trajectories were extracted and structurally aligned. The bacterial crystal structure 1GPW.pdb, with the closed loop, is shown in gray. The wild type, K181A-D98A, and T104A snapshots are colored according to *Q*, a measure of structural homology. The snapshot from T104A shows the most open flexible loop conformation. (C) The final and initial snapshots from the wild-type PRFAR undocking simulations were extracted, stucturally aligned, and colored by *Q*. Secondary structure elements for the final snapshot are underlined. Motion in several areas illustrates the hinge-opening motion; glutaminse domain helices 1, 2, and 3 all undergo shifting motions in concert with cyclase domain helices 2, 3, and 4. White arrows illlustrate the relative shift in helices *h*α2 and *f*α4, as well as *h*α1 and *f*α3. A loop in the glutaminase domain, composed of residues *h*L90−*h*N109 also demonstrates significant rearrangement upon PRFAR undocking.

tions for the *T. maritima* isoform (*15*). The crystal structures of the yeast isoform also indicate that this loop is flexible and dynamic, as it was missing clear electron density in all of the available yeast structures (*14*, *54*). The structural transition between the open, apo state and the closed, active state appears to be associated with the binding of the PRFAR substrate within the cyclase active site. Therefore, it is of interest to report the loop dynamics during the PRFAR undocking simulations.

All of the systems exhibit loop opening motion during the undocking simulations, and the range of flexible loop motion is presented in Figure 9B. Compared to the *T. maritima* crystal structure, which has the loop resolved in a closed, ordered conformation, the largest loop-opening motion exhibited in the trajectories occurred in the *f*T104A mutant. This result is consistent with the fact that loss of the *f*T104 hydroxyl group allows PRFAR to interact more with the flexible loop upon removal. It is worthwhile to note that, although the flexible loop opens to allow PRFAR to exit from the cyclase active site, the secondary structure motifs within the ordered loop remained largely intact. However, the simulations clearly indicate that the region of lowest structural stability is within the PRFAR binding site (Figure 9A,B). These results support the notion that regions of low stability within the binding sites of allosterically regulated proteins are important for the transmission of information to distal sites (*55*, *56*).

3. DISCUSSION

3.1. Structural Transitions between Functional States in IGP Synthase. According to allosteric theory, binding of the effector can enable enzyme activity by selectively stabilizing the subensemble of active states over the inactive states (*2*). In IGP synthase, the binding of the allosteric effector PRFAR to the cyclase active site induces a structural rearrangement of the *f*β1−*f*α1 flexible loop, from a disordered state to a

β-hairpin state. From the crystallographic information and the SMD simulations, it is clear that this region exhibits the lowest degree of structural stability in the enzyme complex. The PRFAR undocking simulations and the correlated motion analysis indicate that the structural rearrangement of the PRFAR binding site, including the opening motion of the flexible loop, is coupled to a cooperative transition at the interface. In the wild-type simulations, prominent interface opening movements are correlated to removal of each of the two PRFAR phosphate groups. This behavior is consistent with established kinetic studies, which indicated that binding of PRFAR and not the individual monophosphate substrates is required for full glutaminase stimulation (*13*).

By extension, we propose that the reverse process, that is, the binding of the allosteric effector PRFAR to the cyclase active site, results in an overall tightening of the interface due to increased electrostatic interactions at the hisH and hisF interface (*25*) and correlated motions in the protein. Furthermore, the hinge-closing motion at the interface could induce a structural rearrangement of the unformed oxyanion hole within the glutaminase active site, which has been suggested to play an integral role in the regulation of glutaminase activity (*13, 14*).

The principal component analysis indicates significant differences in the motion captured by the dominant PCs depending on whether or not PRFAR is bound to hisF. Although the breathing motion at the interface is present in both simulations, it is drastically reduced in the closed T state. The presence of PRFAR reduces the motion in the loops at the active site of hisF due to hydrogen bond and salt bridge interactions between the residues in the hisF active-site loops and the substrate. Furthermore, in the closed T state, the motion within the hisF flexible loops is strongly coupled to the interface opening motion, indicating the ability of PRFAR to effect an allosteric transition at a specific location (the interface) that is distal from the hisF active site. Normal mode analysis with the elastic network model indicates that a few low energy normal modes contribute significantly to the transition from the R to the T state, as shown in the Supporting Information.

3.2. The Conserved Allosteric Network Exhibits Correlated Motion. The correlation analysis presented here indicates that the conserved residues within the proposed allosteric network exhibit correlated motion during the allosteric transition. Our analysis indicates that, within proteins of a single functionality, the residues involved in the allosteric regulation can be identified by coupling evolutionary profiles with a dynamic correlation analysis. It is also possible that the network of conserved residues may form parallel pathways for signal transduction. In the case of IGP synthase, some of the residues in the proposed allosteric network have already been shown to play a role in the ammonia channeling event (*16*−*18*). It is possible that some residues within the channel play dual roles, functioning to assist both the ammonia transport as well as the allosteric signal.

3.3. Main Relay Points in the Allosteric Signaling Pathway. In IGP synthase, an evolutionarily conserved pathway of residues connects the allosteric site where PRFAR binds and the glutaminase active site, spanning a distance of 30 Å (Figure 1 and Supporting Information Figures 12 and 13). The residues within the conserved network likely serve to assist in the conduction of ammonia or are involved in the communication of stress, which is initiated on effector binding at the allosteric site. Using a combination of biochemical and computational experiments, the role of specific residues in the formation of a conserved network of interactions is elucidated.

Flexible Loop Residue fK19 Forms a Critical Interaction with PRFAR. In the various crystal structures of the protein complex, *f*K19 is seen in multiple conformations, at times forming salt bridges with *f*D11 and *f*D176 or forming hydrogen bonds with various surrounding groups. In our undocking simulations, *fK*19 makes one of the longest lived contacts with the glycerol phosphate group of PRFAR. The flexibilty of the loop contributes to the persistence of this contact, as it allows major large scale motions of *f*K19 as PRFAR is undocked.

On the basis of the experimental kinetic assays, the available crystal structures, and the SMD simulations, we propose that formation of the salt bridge between *f*K19 and the glycerol phosphate group of PRFAR assists in the transition of the flexible loop from the disordered to ordered state. Electrostatic maps of the C-terminal end of hisF indicate that *f*K19 contributes to the positive electrostatic potential in the glycerol phosphate binding side (Supporting Information Figure 14). After the cyclase reaction takes place, product IGP unbinding disrupts this local electrostatic network, reducing the structural rigidity of this region. The formation and disruption of this local network of interactions upon effector binding/unbinding is proposed to play a role in the allosteric signal transmission.

Phosphate Binding Site Residue fT104 Relays PRFAR Binding Signal. On the opposite side of the binding site, *f*T104 forms an important contact with the ribose phosphate of PRFAR and strand *f*β4. It is clear from the kinetic assays and SMD simulations (Figures 5 and 7) that the hydroxyl group of *f*T104 has the strongest correlation in motion to rP and could be involved in allosteric signal transmission as PRFAR docks or undocks.

Electrostatic maps of apo-IGP synthase indicate an increased positive potential within the *f*T104 binding site, as compared to a noticeably weaker positive potential at the glycerol phosphate binding site (Supporting Information Figure 14). HisA, the enzyme catalyzing the previous step in the pathway, binds a substrate with two perfectly symmetric ribose phosphate groups. Comparisons of the electrostatic maps of hisA and hisF in Supporting Information Figure 14 show that this symmetry is also reflected in the map at the C-terminus. HisF, which binds the asymmetric PRFAR, exhibits a more asymmetric electrostatic potential, which may be large enough to steer the ribose phosphate group into the *f*T104 binding site first.

Conserved Residues Anchor the Interface. The glutaminase active site is formed at the interface of the two domains and is in prime position to be regulated by signal propagated through the cyclase domain. The interdomain salt bridge formed by *h*K181 and *f*D98 stabilizes the interface by providing a long-lasting, static contact between the two subunits; however, because it is directly adjacent to the glutaminase active site, it may also serve as a conduit to transmit dynamic information during the course of the enzymatic reaction. Nearby conserved residues *h*N15 (S16 in yeast) and *h*N12 make close hydrogen bond contacts with

the interdomain salt bridge, providing an additional degree of rigidity to the glutaminase active site (Figure 4 in ref 18).

In the *T. maritima* isoform, *h*N15 is structurally equivalent to N13 in yeast. *h*N15 resides near the end of *h*α1, and mutation of this group to alanine decreases the competence of the allosteric signal to only 100-fold over basal levels. Mutation of *h*N15 to alanine removes two hydrogen bonds with the interdomain salt bridge, therefore decoupling this important helix from the glutaminase active site and *f*β4 strand, resulting in a reduction of the competence of allosteric signal transmission.

Similarly, the *h*K181−*f*D98 interdomain salt bridge plays a key role in mediating the allosteric signal initiated upon PRFAR binding, as removal of this contact reduces the competence of the allosteric signal to only 180-fold over basal levels. This salt bridge is one of the central components stabilizing the interface. It forms a connection between the *h*α1 helix housing *h*N15, the glutaminase active site, and *h*α2. Removal of this stabilizing contact seems to make the interface more flexible and independent of the allosteric signal. Loss of this salt bridge could lead to complete dissociation of the complex, which would likely occur on the microsecond to millisecond time scale or slower. We can only speculate that this may be a contributing factor to the uncoupling of the two reactions seen experimentally, as those time scales are not accessible in the simulations presented here.

3.4. Proposed Mechanism and Suggestions for Future Work. From the available biochemical kinetic assays, crystal structures, SMD simulations, correlated motion analysis, and the principal component analysis, a network of interactions regulating the allosteric signal in IGP synthase is revealed, allowing us to offer the following overall reaction scenario. Initially, the enzyme, glutamine, and PRFAR are in the free, unbound states. Glutamine, present in relatively high concentrations within the cell, gains access to the glutaminase active site via the hinge-open area near helices *h*α1, *h*α2, *f*α3, and *f*α4. Although it has been found that the substrates bind in any order (*13*), most likely a large population of the inactive conformers have glutamine bound, due to its significantly higher cellular concentration. PRFAR, the product of the previous step in the histidine biosynthesis pathway, is produced and drawn into the cyclase active site because of electrostatic interactions between its two phosphate groups and the positive electrostatic potential on the C-terminus of the cyclase domain (Supporting Information Figure 14). *f*K19 on the flexible loop may make initial contact with the glycerol phosphate group, acting similar to a fly-casting mechanism (*57*), and as the ribose phosphate moiety is drawn toward its phosphate binding site, the flexible loop is brought closer to the nucleotide substrate. Binding of PRFAR within the cyclase active site induces a structural transition of the *f*β1−*f*α1 flexible loop from a disordered to an ordered state. This structural transition, coupled with the desolvation of the PRFAR binding site and energetically favorable contacts between the ligand (PRFAR) and conserved residues within the binding site, releases binding energy that initiates the allosteric signal transduction.

In the active Michaelis complex, the fully docked PRFAR makes five salt bridges and at least ten hydrogen bonds with conserved residues within the cyclase active site, and an estimate of the favorable nonbonded interaction energy between PRFAR and the cyclase domain is in excess of −200 kcal/mol (Figure 2). Near the glycerol phosphate binding site, *f*K19 acts as a key initiator of the allosteric signal through the formation of salt bridges with the glycerol phosphate group of PRFAR and nearby D11. Another important interaction is provided by the hydroxyl group of *f*T104, as it forms a long-lasting hydrogen bond with the ribose phosphate group and provides a direct link between the allosteric effector and *f*β4 of the cyclase domain. Mutation of either of these groups to alanine alters the PRFAR docking dynamics and corresponding cyclase domain dynamics (Figures 7 and 9), resulting in a marked reduction of the competence of the allosteric signal to the glutaminase site (Table 1). The enhanced structural rigidity of the cyclase active site upon PRFAR binding is communicated directly through the cyclase domain and into the interface via a network of evolutionarily conserved residues on strands (Figure 1).

At the interface region close to strand *f*β1 is the cation−π interaction between *h*W123 and *f*R249. In the yeast isoform, this interaction is near the covalent linker attaching the two domains. In addition to forming a stabilizing contact at the interface, the cation−π interaction also serves as a molecular hinge. At the interface region close to strand *f*β4, *f*D98 forms a critical interdomain contact with *h*K181. This salt bridge, adjacent to the glutaminase active site, anchors the interface in this region and enhances the structural stability of the glutaminase active site. The *h*K181−*f*D98 salt bridge anchor directs the PRFAR docking forces to other regions of the interface that are less tightly bound, thus acting as a conduit of information. It is postulated that a subtle upward push resulting from the interface tightening upon PRFAR binding is transmitted through this contact, causing the oxyanion hole to adopt the proper conformation for glutamine hydrolysis. Two additional conserved residues, *h*N12 and *h*N15 of the glutaminase domain, interact with the interdomain salt bridge throughout the allosteric event. Alternating hydrogen bonds between the *h*N15 side chain and the interdomain salt bridge increase the structural rigidity of the glutaminase active site.

During the glutaminase catalytic event, the network of interdomain contacts maintains close interactions in the *h*α1, *h*α2, *f*α3, and *f*α4 region. Two conserved glutamine residues, *f*Q123 in the *f*α4−*f*β5 loop and *h*Q88 in the nucleophilic elbow, stabilize the covalently bound glutamyl thioester intermediate, which enhances catalysis (*18*). Ammonia is released and diffuses across the interface of the two proteins through a side opening and into the core of the $(\beta/\alpha)_8$ barrel (*16*) and is able to act as a nucleophile in the next reaction. The full ammonia conduction event is predicted to take a few hundred nanoseconds (*17*, *25*). After the cyclase reaction is complete, AICAR and IGP dissociate from their respective phosphate binding sites. During the IGP and AICAR unbinding events, the disruption of the *f*K19−IGP salt bridge and the *f*T104 hydrogen bond to the phosphate group of AICAR is communicated through the conserved network of contacts, stimulating the hinge-opening motion at the interface. While the complex is in its hinge-open formation, bulk waters flush out the interface, allowing release of the glutamate product and reentry of a new glutamine molecule, which reinitiates the enzymatic cycle.

Although we present a comprehensive mechanism for the transmission of the allosteric signal in IGP synthase, ad-

ditional experiments could be employed to further probe the controlled regulation of the enzyme and verify our theory. Despite the fact that the mutagenesis experiments for this enzyme have been quite exhaustive, additional, select mutants at regions distal to the glutaminase active site could still be useful: a double mutation of the cation−π interaction (*h*W123A−*f*R249A) and any additional mutations along the conserved network presented in Figure 1 and Supporting Information Figure 12 would likely disrupt the communication pathway between the two distal sites. Engineering a disulfide bridge or phosphate linkers between the two domains in the area of the hinge-opening motion should incapacitate the enzyme, as it would not allow the entrance of glutamine substrate into the glutaminase active site (e.g., *h*G52S−*f*F120S). Unfortunately, fluorescence resonance energy transfer (FRET) applications would not be feasible as the hinge-opening and hinge-closing motion occurs on a length scale that is too small to resolve (domain−domain movement of approximately 10−15 Å) unless the fluorophores could be placed along the periphery of the domain away from the interface on the hinge. However, NMR experiments coupled with computational methods could be employed to ascertain the rates of conformational dynamics and how they correlate to rates of substrate turnover or, in other words, to characterize the molecular switch of the flexible loop and monitor the domain−domain opening and closing movement at the interface. NMR has already been elegantly and successfully employed to elicit the relationship between enzyme function and dynamics including flexible loop motion in triose phosphate isomerase (*58*) and dihydrofolate reductase (*59*) and a nucleotide-binding lid in adenylate kinase (*60*); thus, NMR is a particularly promising approach for further studies of IGP synthase. Finally, site-direct spin labeling used in combination with electron paramagnetic resonance (EPR) spectroscopy could also be a viable option to probe the domain−domain conformational changes and shifts in secondary structure elements associated with the hinge-opening motion ((*61*) and references therein). Having used molecular dynamics and correlation analysis to show that the transmission of the allosteric signal in IGPS could be carried out by a network of conserved interactions, examining the evolutionary profiles of other GATs that show significant allostery should be a first step in identifying the communication pathway of these systems.

ACKNOWLEDGMENT

We thank the Luthey-Schulten group members for many helpful discussions. Special thanks to Elizabeth Villa at the NIH Center for Macromolecular Modeling and Bioinformatics for assistance with the creation of the SMD movie presented in the online Supporting Information. Molecular images were created with the graphics program VMD (*28*). The authors are grateful to NCSA for their gracious support. This work was funded by National Science Foundation grants (MCB02-35144 and MCB04-46227) and a National Resource Allocation Committee grant (MCA03-50275) (both to Z.L.-S.) as well as a National Institute of Health grant (RO1 GM067195) to V.J.D.

SUPPORTING INFORMATION AVAILABLE

Two Supporting Information files are available online. The first is the supplemental information file which describes the normal mode analysis with the elastic network model; it also contains additional figures referred to in the text. We also supply a representative movie of a PRFAR undocking trajectory. This material is available free of charge via the Internet at http://pubs.acs.org.

REFERENCES

1. Changeux, J., and Edelstein, S. J. (2005) Allosteric mechanisms of signal transduction, *Science 308*, 1424−1428.
2. Monod, J., Changeux, J., and Jacob, F. (1963) Allosteric proteins and cellular control systems, *J. Mol. Biol. 6*, 306−329.
3. Tesmer, J. J., Klem, T. J., Deras, M. L., Davisson, V. J., and Smith, J. L. (1996) The crystal structure of GMP synthetase reveals a novel catalytic triad and is a structural paradigm for two enzyme families, *Nat. Struct. Biol. 3*, 74−86.
4. Raushel, F. M., Thoden, J. B., and Holden, H. M. (1999) The Amidotransferase Family of Enzymes: Molecular Machines for the Production and Delivery of Ammonia, *Biochemistry 38*, 7891−7899.
5. Oshikane, H., Sheppard, K., Fukai, S., Nakamura, Y., Ishitani, R., Numata, T., Sherrer, R. L., Feng, L., Schmitt, E., Panvert, M., Blanquet, S., Mechulam, Y., Söll, D., and Nurekir, O. (2006) Structural basis of RNA-dependent recruitment of glutamine to the genetic code, *Science 312*, 1950−1954.
6. Roux, B., and Walsh, C. T. (1992) *ρ*-Aminobenzoate Synthesis in *Escherichia coli*: Kinetic and Mechanistic Characterization of the Amidotransferase PabA, *Biochemistry 31*, 6904−6910.
7. Chaparian, M. G., and Evans, D. R. (1991) The catalytic mechanism of the amidotransferase domain of the syrian hamster multifunctional protein cad, *J. Biol. Chem. 266*, 3387−3395.
8. Willemoes, M. (2003) Thr-431 and Arg-433 are part of a conserved sequence motif of the glutamine amidotransferase domain of CTP synthetases and are involved in GTP activation of *Lactococcus lactis* enzyme, *J. Biol. Chem. 278*, 9407−9411.
9. Nakamura, J., Straub, K., Wu, J., and Lou, L. (1995) The glutamine hydrolysis function of human GMP synthetase, *J. Biol. Chem. 270*, 23450−23455.
10. Zalkin, H., and Smith, J. L. (1998) Enzymes utilizing glutamine as an amide donor, *Adv. Enzymol. Relat. Areas Mol. Biol. 72*, 87−144.
11. Lobley, G. E., Hoskin, S. O., and McNeil, C. J. (2001) Glutamine in animal science and production, *J. Nutr. 131*, 2525S−2531S.
12. Haussinger, D., Lang, F., and Gerok, W. (1994) Regulation of cell function by the cellular hydration state, *Am. J. Physio. 267*, E343−E355.
13. Myers, R. S., Jensen, J., Deras, I., Smith, J. L., and Davisson, V. J. (2003) Substrate-Induced Changes in the Ammonia Channel for Imidazole Glycerol Phosphate Synthase, *Biochemistry 42*, 7013−7022.
14. Chaudhuri, B. N., Lange, S. C., Myers, R. S., Davisson, V. J., and Smith, J. L. (2003) Toward Understanding the Mechanism of the Complex Cyclization Reaction Catalyzed by Imidazole Glycerolphosphate Synthase: Crystal Structures of a Ternary Complex and the Free Enzyme, *Biochemistry 42*, 7003−7012.
15. Douangamath, A., Walker, M., Beismann-Driemeyer, S., Vega-Fernandez, M., Sterner, R., and Wilmanns, M. (2002) Structural evidence for ammonia tunneling across the $(\beta/\alpha)_8$ barrel of imidazole glycerol phosphate synthase bienzyme complex, *Structure 10*, 185−193.
16. Amaro, R. E., Myers, R. S., Davisson, V. J., and Luthey-Schulten, Z. A. (2005) Structural elements exclude water to optimize ammonia transfer in IGP synthase, *Biophys. J. 89*, 475−487.
17. Amaro, R., Tajkhorshid, E., and Luthey-Schulten, Z. (2003) Developing an energy landscape for the novel function of a $(\beta/\alpha)_8$ barrel: Ammonia conduction through hisF, *PNAS 100*, 7599−7604.
18. Myers, R. S., Amaro, R. E., Luthey-Schulten, Z. A., and Davisson, V. J. (2005) Reaction Coupling through Interdomain Contacts in Imidazole Glycerol Phosphate Synthase, *Biochemistry 44*, 11974−11985.
19. Suel, G. M., Lockless, S. W., Wall, M. A., and Ranganathan, R. (2002) Evolutionarily conserved networks of residues mediate allosteric communication in proteins, *Nat. Struct. Mol. Bio. 10*, 59−68.

20. Zheng, W., Brooks, B. R., Doniach, S., and Thirumalai, D. (2005) Network of dynamically important residues in the open/closed transition in polymerases is strongly conserved, *Structure 13*, 565−577.
21. Thoden, J. B., Huang, X., Raushel, F. M., and Holden, H. M. (1999) The Small Subunit of Carbamoyl Phosphate Synthetase: Snapshots along the Reaction Pathway, *Biochemistry 38*, 16158−16166.
22. MacKerell, A. D., Jr., Bashford, D., Bellott, M., Dunbrack, R. L., Evanseck, J. D., Field, M. J., Fischer, S., Gao, J., Guo, H., Ha, S., Joseph-McCarthy, D., Kuchnir, L., Kuczera, K., Lau, F. T. K., Mattos, C., Michnick, S., Ngo, T., Nguyen, D. T., Prodhom, B., Reiher, W. E., III, Roux, B., Schlenkrich, M., Smith, J. C., Stote, R., Straub, J., Watanabe, M., Wiorkiewicz-Kuczera, J., Yin, D., and Karplus, M. (1998) All-Atom Empirical Potential for Molecular Modeling and Dynamics Studies of Proteins, *J. Phys. Chem. B 102*, 3586−3616.
23. MacKerell, A. (2003) Workshop on methods and applications of molecular dynamics to biopolymers, http://www.psc.edu/general/software/packages/charmm/tutorial/index.html.
24. MacKerell, A. (2003) Strategies for parameter development in CHARMM, http://www.psc.edu/general/software/packages/charmm/tutorial/mackerell/PARAM_00.pdf
25. Amaro, R., and Luthey-Schulten, Z. (2004) Molecular dynamics simulations of substrate channeling though an alpha-beta barrel protein, *Chem. Phys. 307*, 147−155.
26. Amaro, R., Daliwal, B., and Luthey-Schulten, Z. (2004) Parameterizing a novel residue, http://www.ks.uiuc.edu/training/tutorials/.
27. Grubmüller, H. (1996) *Solvate*, Theoretical Biophysics Group, Institute for Medical Optics, Ludwig-Maximilians University, Munich, Version 1.0.
28. Humphrey, W., Dalke, A., and Schulten, K. (1996) VMD−Visual Molecular Dynamics, *J. Mol. Graphics 14*, 33−38.
29. Feller, S., Zhang, Z., Pastor, R., and Brooks, B. (1995) Constant pressure molecular dynamics simulation: The Langevin piston method, *J. Chem. Phys. 103*, 4613−4621.
30. Darden, T., York, D., and Pedersen, L. (1993) Particle mesh Ewald: An N.log(N) method for Ewald sums in large systems, *J. Chem. Phys. 98*, 10089−10092.
31. Grubmüller, H., Heller, H., Windemuth, A., and Schulten, K. (1991) Generalized Verlet algorithm for efficient molecular dynamics simulations with long-range interactions, *Mol. Simul. 6*, 121−142.
32. Schlick, T., Skeel, R., Brunger, A., Kale, L., Board, J. A., Hermans, J., and Schulten, K. (1999) Algorithmic challenges in computational molecular biophysics, *J. Comp. Phys. 151*, 9−48.
33. Phillips, J. C., Braun, R., Wang, R., Gumbart, J., Tajkhorshid, E., Villa, E., Chipot, C., Skeel, R. D., Kale, L., and Schulten, K. (2005) Scalable Molecular dynamics with NAMD, *J. Comput. Chem. 26*, 1781−1802.
34. Jorgensen, W. L., Chandrasekhar, J., Madura, J. D., Impey, R. W., and Klein., M. L. (1983) Comparison of simple potential functions for simulating liquid water, *J. Chem. Phys.* 79, 926−935.
35. Isralewitz, B., Baudry, J., Gullingsrud, J., and Schulten, D. K. (2001) Steered molecular dynamics investigations of protein function, *J. Mol. Graphics Modell. 19*, 13−25.
36. Krammer, A., Lu, H., Isralewitz, B., Schulten, K., and Vogel, V. (1999) Forced unfolding of fibronectin type III module reveals a tensile molecular recognition switch, *Proc. Natl. Acad. Sci. U.S.A. 96*, 1351−1356.
37. Gao, M., Craig, D., Lequin, O., Campbell, I., Vogel, V., and Schulten, K. (2003) Structural and functional significance of mechanically unfolded fibronectin type III intermediates, *Proc. Natl. Acad. Sci. U.S.A. 100*, 14784−14789.
38. Autenrieth, F., Tajkhorshid, E., Schulten, K., and Luthey-Schulten, Z. (2004) Role of water in transient cytochrome c2 docking, *J. Phys. Chem. B 108*, 20376−20387.
39. Aksimentiev, A., Balabin, I., Fillingame, R., and Schulten, K. (2004) Insights into the molecular mechanism of rotation in the f_0 sector of ATP synthase, *Biophys. J. 86*, 1332−1344.
40. Jarzynski, C. (1997) Equilibrium free-energy differences from nonequilibrium measurements: A master-equation approach, *Phys. Rev. E 56*, 5018−5035.
41. Jarzynski, C. (1997) Nonequilibrium equality for free energy differences, *Phys. Rev. Lett. 78*, 2690−2693.
42. Park, S., Khalili-Araghi, F., Tajkhorshid, E., and Schulten, K. (2003) Free energy calculation from steered molecular dynamics simulations using Jarzynski's identity, *J. Chem. Phys. 119*, 3559−3566.
43. Garcia, A. E. (1992) Large-amplitude nonlinear motions in proteins, *Phys. Rev. Lett. 68*, 2696−2699.
44. Hayward, S., Kitao, A., and Go, N. (1994) Harmonic and anharmonic aspects in the dynamics of BPTI: a normal mode analysis and principal component analysis, *Protein Sci. 3*, 936−943.
45. Balsera, M. A., Wriggers, W., Oono, Y., and Schulten, K. (1996) Principal component analysis and long time protein dynamics, *J. Phys. Chem. 100*, 2567−2572.
46. Caves, L. S. D., Evanseck, J. D., and Karplus, M. (1998) Locally accessible conformations of proteins: multiple molecular dynamics simulations of crambin, *Protein Sci. 7*, 649−666.
47. Tai, K., Shen, T., Börjesson, U., Philppopoulos, M., and McCammon, J. A. (2001) Analysis of a 10-ns molecular dynamics simulation of mouse acetylcholinesterase, *Biophys. J. 81*, 715−724.
48. Eargle, J., Roberts, E., Wright, D., and Luthey-Schulten, Z. (2006) Multiseq: unifying sequence and structure data for evolutionary analysis. *BMC Bioinformatics 7*, 382.
49. Russel, R. B., and Barton, G. J. (1992) Multiple protein sequence alignment from tertiary structure comparison: Assignment of global and residue confidence levels, *Proteins: Struc., Funct., Genet. 14*, 309−323.
50. Eastwood, M. P., Hardin, C., Luthey-Schulten, Z., and Wolynes, P. G. (2001) Evaluating protein structure-prediction schemes using energy landscape theory, *IBM J. Res. Dev. 45*, 475−497.
51. Ichiye, T., and Karplus, M. (1991) Collective motions in proteins: a covariance analysis of atomic fluctuations in molecular dynamics and normal mode simulations, *Proteins: Struc., Funct., Genet. 11*, 205−217.
52. Hünenberger, P. H., Mark, A. E., and van Gunsteren, W. F. (1995) Fluctuation and cross-correlation analysis of protein motions observed in nanosecond molecular dynamics simulations, *J. Mol. Biol. 252*, 492−503.
53. Young, M. A., Gongloni, S., Superti-Furga, G., Roux, B., and Kuriyan, J. (2001) Dynamic coupling between the SH2 and SH3 domains of c-Src and Hck underlies their inactivation by C-terminal tyrosine phosphorylation, *Cell 105*, 115−126.
54. Chaudhuri, B., Lange, S., Myers, R., Chittur, S., Davisson, V. J., and Smith, J. L. (2001) Crystal structure of imidazole glycerol phosphate synthase: A tunnel through a $(\beta/\alpha)_8$ barrel joins two active sites, *Structure 9*, 987−997.
55. Freire, E. (1999) The propagation of binding interactions to remote sites in proteins: Analysis of the binding of the monoclonal antibody D1.3 to lysozyme, *Proc. Natl. Acad. Sci. U.S.A. 96*, 10118−10122.
56. Luque, I., and Freire, E. (2000) Structural stability of binding sites: Consequences for binding affinity and allosteric effects, *Proteins: Struc., Funct., and Gen. 41*, 63−71.
57. Shoemaker, B., Portman, J., and Wolynes, P. (2000) Speeding molecular recognition by using the folding funnel: The fly-casting mechanism, *PNAS 97*, 8868−8873.
58. Rozovsky, S., Jogl, G., Tong, L., and McDermott, A. E. (2001) Solution-state nmr investigations of triosephosphate isomerase active site loop motion: Ligand release in relation to active site loop dynamics, *J. Mol. Biol. 310*, 271−280.
59. Venkitakrishnan, R. P., Zaborowski, E., McElheny, D., Benkovic, S. J., Dyson, H. J., and Wright, P. E. (2004) Conformational changes in the active site loops of dihydrofolate reductase during the catalytic cycle, *Biochemistry 43*, 16046−16055.
60. Wolf-Watz, M., Thai, V., Henzler-Wildman, K., Hadjipavlou, G., Eisenmesser, E. Z., and Kern, D. (2004) Linkage between dynamics and catalysis in a thermophilic-mesophilic enzyme pair, *Nat. Struct. Biol. 11*, 945−949.
61. Hubbell, W. L., Cafiso, D. S., and Altenbach, C. (2000) Identifying conformational changes with site-directed spin labeling, *Nat. Struct. Biol. 7*, 735−739.
62. Frauenfelder, H., and McMahon, B. (1998) Dynamics and function of proteins: the search for general concepts, *Proc. Natl. Acad. Sci. U.S.A. 95*, 4795−4797.
63. Brooks, B. R., Bruccoleri, R. E., Olafson, B. D., States, D. J., Swaminathan, S., and Karplus, M. (1983) CHARMM: A program for macromolecular energy, minimization, and dynamics calculations, *J. Comp. Chem. 4*, 187−217.

64. Go, N., Noguti, T., and Nishikawa, T. (1983) Dynamics of a small protein in terms of low-frequency vibrational modes, *Proc. Natl. Acad. Sci. U.S.A. 80*, 3696−3670.
65. Levitt, M., Sander, C., and Stern, P. S. (1983) The normal modes of a protein: native bovine pancreatic trypsin inhibitor, *Int. J. Quant. Chem. 10*, 181−199.
66. Bahar, I., Atilgan, A. R., and Erman, B. (1997) Direct evaluation of thermal fluctuations using a single parameter harmonic potential, *Folding Des. 2*, 173−181.
67. Tama, F., Gadea, F. X., Marques, O., and Sanejouand, Y. H. (2000) Building-block approach for determining low-frequency normal modes of macromolecules, *Proteins: Struct., Funct., Genet. 41*, 1−7.
68. Bahar, I., and Rader, A. J. (2005) Coarse-grained normal mode analysis in structural biology, *Curr. Opin. Struct. Biol. 15*, 586−592.
69. Suhre, K., and Sanejouand, Y. H. (2004) Elnemo: a normal mode web-server for protein movement analysis and the generation of templates for molecular replacement, *Nucl. Acids Res. 32*, W610−W614.

BI061708E